sustainability

MDPI

Article

Hydrogen and Battery Energy Storage for Resilient High-Renewable Microgrids: A Multi-Objective Assessment of Cost, Emissions and Employment Under Uncertainty

Xue Li, Haotian Ge *, Jiuming Zhong, Chenxi Fan and Jun Li

Hainan Normal University, Haikou 571158, China; daxueli1107@163.com (X.L.); hnsfdx246@163.com (J.Z.); fanchenxi@hainnu.edu.cn (C.F.); lli3028719969@163.com (J.L.)
* Correspondence: sdutght@163.com

Abstract

Stand-alone microgrids with high renewable shares need storage for daily and multi-day balancing. This study compares hydrogen, battery and hybrid storage in five configurations, with and without diesel backup, for a South African residential load. A bus-resolved mixed-integer linear programming model with open hourly data (2012–2021) trades off cost, diesel emissions and employment by ε-constraint analysis; a robust counterpart covers cost, discount-rate and employment-factor uncertainty and 10 weather years. Per kWh delivered, electricity from the compromise designs cost 0.71–1.29 $/kWh; normalising by generation, which includes 30–45% curtailment, understates it 4–7-fold. The hydrogen–battery hybrid was the least-cost fully renewable option (1.30 versus 1.96 and 2.06 M$ with hydrogen or batteries alone), with the battery cycling daily and the tank providing 71 h of autonomy. Robust designs served the load in all 10 years. The findings held under unit-commitment, reserve and wear constraints and across design years, loads, sites and Monte Carlo samples. Carbon prices at EU ETS levels did not displace battery–diesel supply, whereas a 75% cut in hydrogen equipment costs made the diesel-free hybrid equally cheap. Hydrogen adds the most value as a reserve for prolonged deficits, combined with batteries.

Keywords: hydrogen energy storage; battery energy storage system; hybrid renewable microgrid; multi-objective optimisation; robust optimisation; supply adequacy; curtailment; levelised cost of electricity; employment creation; greenhouse gas mitigation; sustainable energy transition

Check for updates

Academic Editor: Jiang Wu

Received: 16 October 2026
Revised: 9 November 2026
Accepted: 11 November 2026
Published: 13 November 2026

Copyright: © 2026 by the authors. Licensee MDPI, Basel, Switzerland. This article is an open access article distributed under the terms and conditions of the Creative Commons Attribution (CC BY) license.

1. Introduction

The rapid expansion of wind and solar photovoltaic (PV) generation is central to decarbonising electricity supply, but the variability of these resources increases the risk of supply–demand imbalance, curtailment and, in weak or isolated networks, supply interruptions [1,2]. Individual storage technologies rarely cover the full range of timescales involved. Batteries are well suited to intra-day balancing but become costly when sized for multi-day or seasonal deficits, whereas hydrogen energy storage offers large energy capacity and negligible self-discharge at the expense of a lower round-trip efficiency. How the two technologies should be selected and sized to deliver reliable, affordable and low-carbon supply therefore remains an open planning question. Storage decisions are also increasingly linked to the decarbonisation of transport [3] and industry [4,5], which broadens their relevance beyond the power sector.

The question is particularly pressing for communities with limited or unreliable grid access, where electricity supply must also deliver social and economic benefits. In 2023, an estimated 666 million people worldwide still lacked access to electricity [6], while fossil fuels continued to supply about 81.5% of global primary energy [7]. Energy poverty and dependence on fossil fuels aggravate pollution and limit local development [8]. Distributed renewable microgrids have therefore emerged as a practical alternative to grid extension and diesel generation [9], including in transport-energy hubs, such as seaports, where port operations and microgrid energy management are optimised jointly under uncertain renewable supply [10]; however, because renewable output is intermittent, storage and backup capacity are required to guarantee continuous supply.

Hydrogen and battery storage are complementary in principle. Batteries are suited to short-term balancing, whereas hydrogen systems based on electrolysis, storage and fuel cells are better suited to long-duration storage [1,9]. Batteries can absorb daily fluctuations in demand and generation, while surplus renewable electricity can be converted into hydrogen, stored, and later reconverted into electricity or used for other purposes. Beyond the power sector, hydrogen can support the decarbonisation of transport [11], steel and chemicals production [4,5] and sustainable fuel production [12], and the coupling of electrolysers with batteries and renewable generation is expected to accelerate the development of a hydrogen economy [13,14]. Stochastic operations planning has also been used to integrate uncertain renewable supply and demand in electrified container terminals [15]. Renewable deployment has also been associated with economic growth and employment [16,17], and microgrids in remote areas can create jobs in manufacturing, installation, operation and maintenance, linking electricity access with local development [18].

1.1. Related Work

Previous optimisation studies have quantified the trade-offs between cost, emissions and reliability in hybrid renewable systems with hydrogen production and storage [19,20]. Multi-objective approaches have been used to balance competing economic and environmental goals in microgrid planning and operation [21], and demand-side flexibility has been integrated through building-level energy management [22]. Hydrogen-based storage, comprising electrolysers, fuel cells and hydrogen tanks, converts surplus renewable electricity into hydrogen that can be stored and reconverted when needed [23,24]. At larger scales, underground and depleted-reservoir storage has been investigated for long-duration and seasonal applications [25,26], and advances in storage materials and carriers continue to broaden the options [27,28]. In rural and isolated areas, hydrogen systems can reduce reliance on diesel generators and the associated greenhouse gas (GHG) emissions.

Battery energy storage systems (BESS), in turn, remain essential for stabilising renewable-dominated systems because of their fast response and high round-trip efficiency, and their roles in peak shaving, load shifting and frequency regulation are well documented [29]. Nevertheless, degradation, replacement costs and limited storage duration restrict the ability of batteries alone to sustain supply over extended periods. Comparative studies of lithium-ion batteries and reversible solid oxide fuel cells have highlighted the resulting thermoeconomic trade-offs [30], and combined PV–battery–hydrogen systems have been proposed to reach full energy self-sufficiency in buildings [31] and to supply large stand-alone grids with fully renewable electricity [32]. Hydrogen storage has also been shown to mitigate the variability of wind and solar power and thereby support grid stability [33].

Because microgrid planning is exposed to uncertain resources, costs and policies, stochastic and distributionally robust formulations have increasingly been applied to systems with multiple storage technologies [34,35]. At the same time, studies on energy poverty and just transitions emphasize that the social outcomes of energy investments, such

as access, affordability and employment, should be assessed alongside their economic and environmental performance [8,36].

1.2. Research Gaps and Contributions

Despite this progress, three gaps remain. First, social dimensions, in particular employment creation, are rarely included as explicit objectives when sizing hydrogen storage, even though they are central to sustainable development. Second, most planning studies assume static techno-economic parameters and neglect the uncertainty of meteorological, economic and social conditions over the system lifetime. Third, hydrogen-based and battery-based storage are seldom compared within a single framework that evaluates economic, environmental and social performance under both deterministic and uncertain conditions, and comparisons are often based on cost metrics normalised by generated rather than delivered electricity, which favours oversized designs. Closing these gaps is necessary for the effective deployment of storage-supported microgrids in high-renewable settings and for designing policy instruments—such as carbon pricing, renewable portfolio standards and targeted subsidies—that support their scale-up.

To address these gaps, this study develops a multi-objective mixed-integer linear programming (MILP) framework to size stand-alone renewable microgrids equipped with a hydrogen energy storage system (HESS), a BESS, or both, with and without diesel generator (DG) backup, and evaluates them under deterministic and robust optimisation. All results are generated with an openly documented, bus-resolved implementation of the model and open input data, so that every reported quantity can be reproduced (Data Availability Statement). The main contributions are as follows:

1. A comparative framework is developed for five microgrid configurations (RES–HESS–DG, RES–HESS, RES–BESS–DG, RES–BESS and the hybrid RES–HESS–BESS, where RES denotes renewable energy sources) that treats total lifetime cost, GHG emissions and employment creation explicitly through an ε-constraint Pareto analysis with normalised objectives, thereby covering the economic, environmental and social pillars of sustainability.
2. Uncertainty in component and fuel costs, the discount rate and employment factors is treated with a box-uncertainty robust counterpart at four uncertainty levels, while meteorological uncertainty is represented by 10 temporally coherent historical years (2012–2021) that are added through a constraint-generation procedure, avoiding physically implausible combinations of independent hourly extremes.
3. Designs are compared on the basis of electricity actually delivered to the load, together with complete annual energy balances (generation, storage throughput and losses, conversion losses and curtailment) and supply-adequacy indicators obtained by multi-year back-testing, which clarifies the actual roles of hydrogen and battery storage at this scale.
4. The findings are tested under operational and wear constraints, alternative design years, load profiles and sites and joint input uncertainty, and the effects of regulation-based carbon prices and hydrogen cost reductions are quantified; policy and planning implications are derived for scaling storage-supported microgrids, including options for using surplus renewable electricity in other sectors.

The remainder of this paper is organised as follows. Section 2 describes the system configurations, case study data, component models, performance indicators and optimisation formulation. Section 3 presents the deterministic, multi-objective, robust and sensitivity results, followed by the effects of operational and wear constraints, the robustness of the findings and the carbon-pricing and hydrogen-cost scenarios. Section 4 discusses the findings in the light of previous studies, their sustainability and policy implications, and the limitations of the study. Section 5 concludes the paper.

2. Materials and Methods

2.1. System Configurations and Operating Strategy

The study considers a stand-alone hybrid renewable microgrid comprising wind turbines (WT), solar PV arrays, hydrogen and/or battery storage and, optionally, a backup DG (Figure 1). The storage technologies are (i) a BESS based on lithium-ion batteries and (ii) a HESS consisting of a proton exchange membrane electrolyser (PEM-EL), a proton exchange membrane fuel cell (PEM-FC) and a low-pressure hydrogen tank (LPT). The PV array and all storage devices are connected to a DC bus, whereas the wind turbines, the DG and the residential load are connected to an AC bus; a bidirectional converter links the two buses. Five configurations are evaluated: Configuration A (RES–HESS–DG), Configuration B (RES–HESS), Configuration C (RES–BESS–DG), Configuration D (RES–BESS) and Configuration E (RES–HESS–BESS). Configuration E tests directly whether hydrogen and battery storage are complementary when they are co-optimised under identical demand and adequacy constraints.

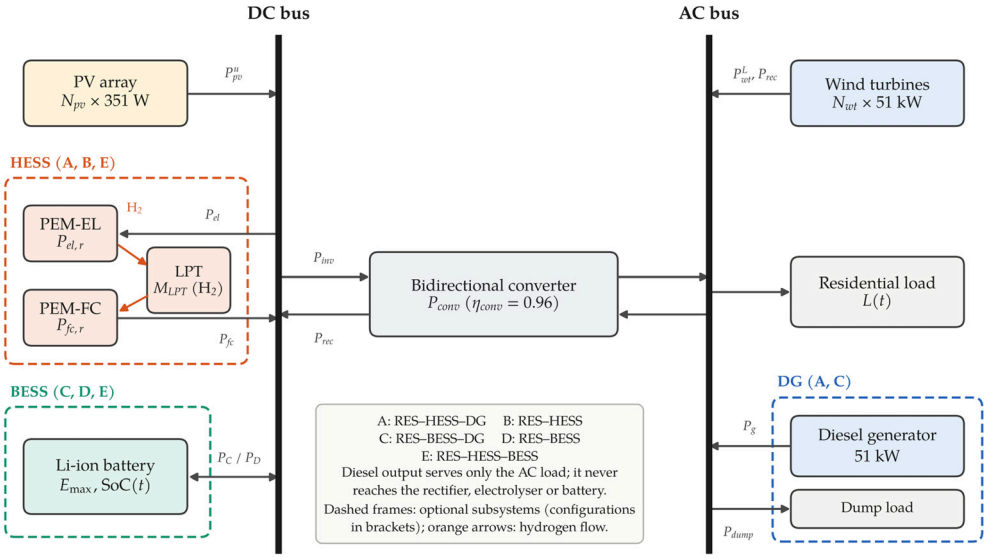


Figure 1. Structure of the hybrid microgrid and the five configurations analysed. PV and storage are connected to the DC bus; wind turbines, the DG and the load are connected to the AC bus. The DG (Configurations A and C) can supply only the AC load, so diesel electricity is never converted into hydrogen or stored in the battery.

Renewable sources are the primary supply in all configurations. The hourly dispatch of all units is co-optimised with the component capacities over the full year (perfect foresight within the year), subject to the rule that the DG may supply only the AC load; diesel electricity can neither be passed through the rectifier nor be used by the electrolyser or the battery, which keeps storage dedicated to renewable surpluses and allows hydrogen-based and battery-based balancing to be compared on an equal footing. Because the microgrid is designed as a stand-alone system, renewable electricity that can be neither consumed nor stored is curtailed, and DG output that exceeds the load when the DG operates at its minimum load is dissipated in a dump load. The load must be met in every hour of the design year (no unserved energy); the adequacy of each design in other years is evaluated separately (Section 2.4.5).

2.2. Case Study and Input Data

Meteorological inputs were obtained from the NASA POWER hourly point service [37] for the grid point at 27.18° S, 28.99° E in the rural north-eastern Free State, about 145 km

south-east of Johannesburg on the South African Highveld. The site is representative of rural farmland with dispersed settlements, where grid extension is costly and supply is weak, i.e., the setting for which stand-alone microgrids are planned, and its open terrain matches the conditions under which wind turbines are installed and for which reanalysis winds are representative. The location combines a high solar resource with a moderate wind resource (mean annual GHI of 2075 kWh/m^2 and mean hub-height wind capacity factor of 25.4% over 2012–2021), so that both generation technologies and both storage technologies are exercised by the optimisation. The hourly series comprise all-sky global horizontal irradiance (GHI), diffuse horizontal irradiance and direct normal irradiance from the CERES SYN1deg product, and 2 m air temperature and 10 m and 50 m wind speeds from the MERRA-2 reanalysis [38]. Time stamps are in local solar time. The availability of diffuse irradiance and of wind speeds at two heights allows plane-of-array irradiance and a site-specific wind-shear exponent (Section 2.3) to be derived directly from the data. The 10 complete years 2012–2021 were used (29 February was removed from leap years to obtain 8760 h per year). The irradiance on a north-facing array tilted at the site latitude (27°) was computed from GHI and diffuse irradiance with the isotropic-sky model (Equation (4)) [39]. The annual GHI ranges from 1983 to 2123 kWh/m^2 across the 10 years and the annual specific PV yield from 1688 to 1777 kWh/kWp; the hub-height wind capacity factor ranges from 23.5% to 27.8%. The year whose PV yield and wind capacity factor are jointly closest to the 10-year medians (2015) is used as the design year for the deterministic optimisation; all 10 years are used in the robust optimisation and in the adequacy back-tests.

The load is represented by the hourly benchmark profile of mature electrified South African households (13 or more years since electrification) from the Domestic Electrical Load (DEL) study, as published in the open delarchetypes repository [40]. The DEL study metered South African households across the country over two decades (1994–2014), and its benchmark profiles are the national reference for residential demand in electrification planning; they reproduce the daily and seasonal pattern of a residential community, with a morning peak, a pronounced evening peak and slightly higher winter demand. The benchmark distinguishes summer and winter (June–September) and weekdays, Saturdays and Sundays. It was mapped onto the calendar of each year and scaled to a mean demand of 20 kW, i.e., an annual consumption of 175.2 MWh with a peak of 36.8 kW, which corresponds to a community of residential buildings or a residence hall and to the 51 kW DG of the reference design. The sensitivity of the results to a ±30% change in demand is reported in Section 3.9. Figure 2 summarises the input data.

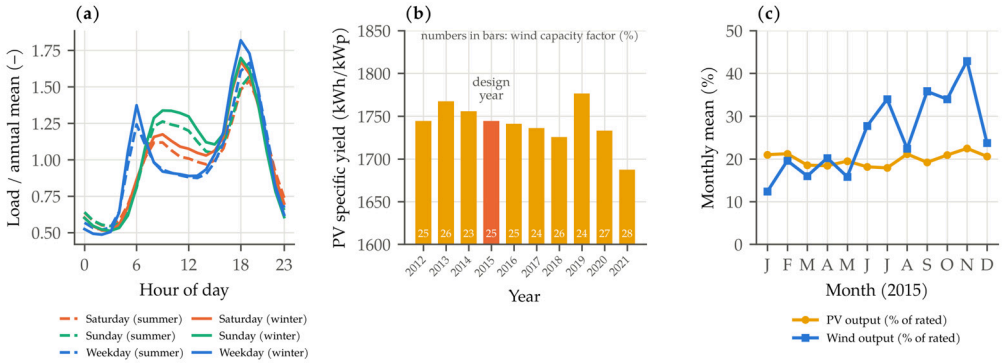


Figure 2. Input data: (**a**) normalised daily load profiles by season and day type; (**b**) annual specific PV yield and wind capacity factor at hub height for 2012–2021 (the design year is highlighted); (**c**) monthly mean PV and wind output per unit of rated capacity in the design year.

2.3. Component Models

2.3.1. Solar Photovoltaic Array

The PV output is calculated from the plane-of-array irradiance and a temperature-dependent conversion efficiency [39]:

$$P_{pv}(t) = f_{pv}\, G_T(t)\, A_{pv}\, \eta_{pv}(t), \tag{1}$$

$$\eta_{pv}(t) = \eta_{pv,ref}\left[1 - \beta_T\left(T_c(t) - T_{ref}\right)\right], \tag{2}$$

$$T_c(t) = T_{amb}(t) + G_T(t)\,\frac{NOCT - 293.15}{800}, \tag{3}$$

$$G_T(t) = (G_h - D_h)\frac{\cos\theta(t)}{\cos\theta_z(t)} + D_h\frac{1+\cos\beta}{2} + \rho\, G_h\frac{1-\cos\beta}{2}, \tag{4}$$

where $P_{pv}(t)$ (W) is the output of one module; $G_T(t)$ (W/m^2) is the in-plane (plane-of-array) irradiance as defined in IEC 61724-1 [41]; A_{pv} (m^2) is the module area; f_{pv} is a lumped derating factor for soiling, mismatch and DC wiring losses (0.85); $\eta_{pv,ref}$ is the module efficiency at standard test conditions (STC: in-plane irradiance of 1000 W/m^2, cell temperature of 25 °C and the AM1.5 reference spectral irradiance of IEC 60904-3 [42]); β_T (1/K) is the magnitude of the temperature coefficient of maximum power (0.46%/K); T_c, T_{ref} and T_{amb} (K) are the cell, reference (298.15 K), and ambient temperatures; NOCT (K) is the nominal operating cell temperature, i.e., the cell temperature at 800 W/m^2, 20 °C ambient temperature and 1 m/s wind speed (the 2016 edition of the IEC 61215 [43] series replaced it by the nominal module operating temperature, NMOT, which is determined under the same conditions at maximum-power operation and can be used in Equation (3) in the same way); G_h and D_h are the global and diffuse horizontal irradiance, respectively; θ_z and θ are the solar zenith angle and the angle of incidence on the array, respectively; β is the tilt angle (not to be confused with the temperature coefficient β_T); and ρ is the ground albedo (0.2). The module has a rated output of 351 W at STC (1000 W/m^2, 25 °C) and an efficiency of 19.04%, corresponding to a module area of 1.843 m^2 ($A_{pv}\eta_{pv,ref} \cdot 1000$ W/m^2 = 351 W).

2.3.2. Wind Turbine

The turbine produces power only between the cut-in and cut-out wind speeds and follows the power curve in Equation (5) [44]. Because wind speed is recorded at a reference height, it is extrapolated to hub height with the power law in Equation (6):

$$P_{wt}(t) = \begin{cases} 0, & v(t) < v_i \text{ or } v(t) \geq v_o \\ P_r\,\frac{v(t)^3 - v_i^3}{v_r^3 - v_i^3}, & v_i \leq v(t) < v_r \\ P_r, & v_r \leq v(t) < v_o \end{cases} \tag{5}$$

$$v_{hub} = v_{ref}\left(\frac{h_{hub}}{h_{ref}}\right)^{\alpha}, \tag{6}$$

where $P_{wt}(t)$ (kW) is the turbine output; P_r (kW) is the rated power; $v(t)$ (m/s) is the hub-height wind speed; v_i, v_r and v_o (m/s) are the cut-in, rated and cut-out wind speeds, respectively; v_{ref} (m/s) is the wind speed at the reference height h_{ref}; h_{hub} (70 m) is the hub height; and α is the wind shear exponent. Because the dataset provides wind speeds at both 10 m and 50 m, the 50 m series is used as reference (h_{ref} = 50 m), which shortens the vertical extrapolation, and the site-specific exponent is derived from the 10-year mean speeds at the two heights ($\alpha = \ln(\bar{v}_{50}/\bar{v}_{10})/\ln 5 = 0.229$). Wind generation complements PV by supplying power at night and during periods of low irradiance.

2.3.3. Electrolyser

A PEM-EL is adopted because of its high conversion efficiency, ability to operate at elevated pressure, high hydrogen purity and good tolerance of fluctuating renewable input [23]. The pressure boundary of the hydrogen chain is defined as follows: the electrolyser stack delivers hydrogen at up to 3 MPa, and the LPT is operated below this outlet pressure, so that no mechanical compressor is required [45]; a pressure regulator reduces the pressure to the fuel-cell inlet, and the energy for drying/purification, water treatment and other balance-of-plant (BoP) loads is included in the system-level efficiency. The electrolyser is supplied only from renewable electricity on the DC bus, and its hydrogen production is

$$\dot{m}_{H_2,a}(t) = \frac{\eta_{el} P_{el}(t)}{HHV_{H_2}}, \tag{7}$$

where $\dot{m}_{H_2,a}(t)$ (kg/h) is the hourly hydrogen production, $P_{el}(t)$ (kW) is the electrolyser power, HHV_{H_2} is the higher heating value of hydrogen (39.4 kWh/kg) and η_{el} is the system-level electrolyser efficiency on an HHV basis (73%), i.e., a specific consumption of 54.0 kWh/kg, including BoP. The stoichiometric water demand is 8.94 kg per kg of hydrogen. Water purification is part of the BoP. With an on-site reverse-osmosis/electrodeionisation unit that recovers 50–75% of the raw water, the raw-water demand is about 12–18 kg per kg of hydrogen. For the compromise designs, this amounts to 22–32 m^3/yr (A), 29–44 m^3/yr (B) and 2–3 m^3/yr (E), i.e., less than the free basic water allocation of a single South African household (6 kL per month). The purification energy, a few kWh per m^3 or less than 0.2 MWh/yr, is covered by the BoP share of the system-level efficiency. In the water-stressed Highveld, the feed water would be drawn from a borehole or from rainwater harvested on the plant roof. Its availability, the disposal of the reject brine and the cost of the water-treatment unit, which is not included in Table 1, should be verified in project development.

Table 1. Cost assumptions for the microgrid components (constant US dollars).

Component	Investment Cost	Replacement Cost	Annual O&M Cost	Lifetime	Multiplier k
Wind turbine conversion system	1050 $/kW	1050 $/kW	2.3% of investment	21 years	2.38
Solar PV modules	2050 $/kW	2050 $/kW	3% of investment	21 years	2.38
Converter	626 $/kW	626 $/kW	13.6 $/kW	16 years	2.38
PEM-FC	2550 $/kW	889 $/kW	0	40,050 h	2.38
PEM-EL	1550 $/kW	1050 $/kW	21 $/kW	16 years	2.38
Hydrogen storage tank (LPT)	666 $/kg	401 $/kg	4 $/kg	16 years	2.09
Diesel generator	221 $/kW	221 $/kW	0.04 $/h per kW rated	15,050 h	2.38
Lithium-ion battery storage	214 $/kWh	214 $/kWh	5.27 $/kWh	11 years	2.38

Lifetimes in hours refer to operating hours (equivalent full-load hours for the fuel cell); replacement costs of the DG and the fuel cell are charged per operating hour. The multiplier k is applied to investment and replacement costs (Section 2.4.1); results without multipliers (k = 1) are given in Section 3.9. Salvage values follow straight-line depreciation of the last installed unit (Equation (21)).

2.3.4. Fuel Cell

A PEM-FC is used because it is suitable for stationary generation, responds quickly to load changes and operates at low temperature (below 100 °C) [31]. The fuel cell reconverts stored hydrogen into DC electricity when renewable output is insufficient:

$$P_{fc}(t) = \eta_{fc} \dot{m}_{H_2,d}(t) LHV_{H_2}, \tag{8}$$

where $\dot{m}_{H_2,d}(t)$ (kg/h) is the hourly hydrogen consumption, $LHV_{H_2} = 33.33$ kWh/kg is the lower heating value and η_{fc} is the net system efficiency of the fuel cell on an LHV basis (50%). Stationary PEM systems achieve net AC efficiencies of about 34–45% (LHV) [46], and pure-hydrogen operation without fuel processing justifies the somewhat higher value adopted here. With these values, the electricity-to-electricity efficiency of the hydrogen chain is 16.7/54.0 = 31%, and its effect on the results is examined over a range of 25–52% in Section 3.9.

2.3.5. Bidirectional Converter

The converter transfers power in both directions between the DC and AC buses. The inverter flow $P_{inv}(t)$ (DC→AC) and the rectifier flow $P_{rec}(t)$ (AC→DC) are modelled as separate non-negative variables, each with an efficiency of $\eta_{conv} = 96\%$ and each limited by the converter rating P_{conv} (kW), which is a decision variable (Equation (18)). The rating is therefore equal to the largest hourly transfer in either direction, and the conversion losses are counted on the energy that actually passes through the converter.

2.3.6. Low-Pressure Hydrogen Tank

The LPT acts as an intermediate buffer between the electrolyser and the fuel cell. It stores hydrogen when production exceeds demand and releases it when fuel-cell demand increases [31]. Its mass balance and operating limits are

$$m(t) = m(t-1) + \dot{m}_{H_2,a}(t) - \dot{m}_{H_2,d}(t), \qquad m(0) = m(8760), \tag{9}$$

$$0.05\,M_{LPT} \le m(t) \le M_{LPT}, \qquad P_{el}(t) \le P_{el}^{rated}, \qquad P_{fc}(t) \le P_{fc}^{rated}, \tag{10}$$

where $m(t)$ (kg) is the stored hydrogen mass and M_{LPT} (kg) is the rated tank capacity. Owing to pressure-drop effects, a minimum residual content of 5% of the rated capacity is imposed. The cyclic condition $m(0) = m(8760)$ prevents the model from using hydrogen that it has not produced within the year. In the core model, binary variables for electrolyser and fuel-cell operation are not required. Simultaneous production and consumption of hydrogen would only add losses and is never optimal, which was verified for all solutions.

2.3.7. Battery Energy Storage System

Lithium-ion batteries are selected for their proven reliability, low self-discharge, high round-trip efficiency, deep depth of discharge (DoD, up to 91%), wide market penetration and technical maturity [29]. The stored energy evolves according to [32]

$$SoC(t) = SoC(t-1) + \eta_C\,P_C(t) - \frac{P_D(t)}{\eta_D}, \qquad SoC(0) = SoC(8760), \tag{11}$$

$$(1 - DoD)\,E_{\max} \le SoC(t) \le E_{\max}, \tag{12}$$

$$P_C(t) \le E_{\max}, \qquad P_D(t) \le E_{\max}, \tag{13}$$

where SoC(t) (kWh) is the stored energy; $P_C(t)$ and $P_D(t)$ (kW) are the charging and discharging powers; $\eta_C = 91\%$ and $\eta_D = 86\%$ are the charging and discharging efficiencies, respectively (round-trip efficiency about 78%); $E_{\max}$ (kWh) is the rated capacity; and DoD = 91% is the maximum depth of discharge; the power limit corresponds to a 1C rating. As for the HESS, binary charge/discharge indicators are unnecessary because simultaneous charging and discharging would only increase losses.

2.3.8. Diesel Generator

The DG serves as backup when renewable generation and storage cannot meet the demand. Its hourly fuel consumption and output limits are

$$FC(t) = \varphi\,P_g(t) + \delta\,P_{g,r}\,X_g(t), \tag{14}$$

$$P_{g,\min} X_g(t) \le P_g(t) \le P_{g,r} X_g(t), \qquad X_g(t) \in \{0,1\}, \tag{15}$$

where $\mathrm{FC}(t)$ (L/h) is the hourly fuel consumption; $P_g(t)$ (kW) is the DG output; $X_g(t)$ is its on/off status; $P_{g,r} = 51$ kW is its rated capacity; $\varphi = 0.274$ L/kWh and $\delta = 0.034$ L/h/kW are the slope and intercept of the fuel curve, respectively; and $P_{g,\min} = 0.31\ P_{g,r}$ is the minimum load. The DG replacement cost is charged per operating hour on the basis of its lifetime of 15,050 operating hours (Section 2.4.1).

2.3.9. Bus-Resolved Power Balances

The hourly power balances of the DC and AC buses are

$$P^u_{pv}(t) + P_{fc}(t) + P_D(t) + \eta_{conv} P_{rec}(t) = P_{el}(t) + P_C(t) + P_{inv}(t), \tag{16}$$

$$P^L_{wt}(t) + P_g(t) - P_{dump}(t) + \eta_{conv} P_{inv}(t) = L(t), \tag{17}$$

$$P_{rec}(t) + P^L_{wt}(t) \le N_{wt} P_{wt}(t), \qquad P^u_{pv}(t) \le N_{pv} P_{pv}(t),$$

$$P_{inv}(t) \le P_{conv}, \qquad P_{rec}(t) \le P_{conv}, \tag{18}$$

where $P^u_{pv}(t)$ is the PV power used (the difference to the available output $N_{pv}P_{pv}(t)$ is curtailed), $P^L_{wt}(t)$ is the wind power supplied directly to the load, $P_{dump}(t)$ is the dump-load power and $L(t)$ (kW) is the load. Terms that refer to components absent from a configuration are zero. Because only wind power can be routed to the rectifier, diesel electricity cannot reach the DC bus.

2.4. Performance Indicators

2.4.1. Total Lifetime Cost and Levelised Cost of Electricity

The total lifetime cost (TLC) comprises the initial capital investment and the net present values (NPV) of O&M and replacement costs, plus the NPV of DG fuel, minus the NPV of the salvage value at the end of the project. Electricity costs are expressed per unit of electricity actually delivered to the load, discounted consistently with the costs [47]:

$$TLC = \sum_c \left(IC_c + OM^{NPV}_c + R^{NPV}_c - S^{NPV}_c \right) + FC^{NPV}_{DG}, \tag{19}$$

$$IC_c = P_c\, IC_{0,c}\, k_c, \qquad OM^{NPV}_c = \sum_{n=1}^{N} \frac{P_c\, OM_c}{(1+r)^n}, \tag{20}$$

$$R^{NPV}_c = \sum_{j:\, jL_c < N} \frac{P_c\, R_c\, k_c}{(1+r)^{jL_c}}, \tag{21}$$

$$S^{NPV}_c = \frac{C^{last}_c}{(1+r)^N} \cdot \frac{L_c - \left(N - n^{last}_c\right)}{L_c},$$

$$R^{NPV}_h = \sum_{n=1}^{N} \frac{R_c\, k_c}{(1+r)^n} \cdot \frac{H_c}{L^h_c}, \tag{22}$$

$$FC^{NPV}_{DG} = \sum_{n=1}^{N} \frac{F_p \sum_t FC(t)}{(1+r)^n},$$

$$LCOE_{served} = \frac{TLC}{\sum_{n=1}^{N} \frac{E_{served}}{(1+r)^n}}, \tag{23}$$

$$LCOE_{gen} = \frac{TLC}{N\, E_{gen}},$$

where P_c is the rated capacity of component c; $IC_{0,c}$, OM_c and R_c are its specific investment, annual O&M and replacement costs (Table 1), respectively; k_c is the cost multiplier

(Table 1); L_c is the calendar lifetime; C_c^{last} and n_c^{last} are the cost and year of the last installation, respectively; L_c^h is the lifetime in operating hours of the DG (15,050 h) and the fuel cell (40,050 h); H_c is the annual operating hours (equivalent full-load hours for the fuel cell); F_p is the diesel price; r is the discount rate; $N = 21$ is the years of the project lifetime; E_{served} is the annual electricity delivered to the load and E_{gen} is the annual electricity generated, including curtailed output. Salvage values follow the straight-line depreciation of the last installed unit. Replacements occur at the end of each calendar lifetime (year 16 for the converter, electrolyser and tank, year 11 for the battery), and the replacement of the DG and the fuel cell is charged in proportion to their operating hours. $LCOE_{served}$ is the primary economic indicator; the generation-based value $LCOE_{gen}$, which is common in the literature, is reported for comparison because it rewards curtailed surpluses. Because all configurations serve the same load, the ranking by $LCOE_{served}$ is identical to the ranking by TLC.

The multipliers k_c (2.38 for most components and 2.09 for the hydrogen tank) convert equipment prices into installed costs and combine price escalation with installation and indirect costs. All results are also reported with the multipliers set to 1, i.e., at the listed equipment prices, so that their effect is explicit (Section 3.9). The multipliers are applied to investment and replacement costs; O&M costs are expressed as stated in Table 1. All costs are in constant US dollars, and the discount rate is real.

2.4.2. Greenhouse Gas Emissions, Carbon Tax and Life-Cycle Basis

Direct CO_2 emissions from DG operation and the emissions avoided relative to supply from the national grid are calculated over the project lifetime as

$$CO_2^{DG} = N \sum_{t=1}^{8760} FC(t)\, EF, \qquad \Delta CO_2 = N\, EF_{grid}\, E_{served} - CO_2^{DG}, \tag{24}$$

where EF = 2.68 kg CO_2/L is the direct (tank-to-exhaust) emission factor of diesel, obtained from the IPCC default carbon content of gas/diesel oil (74.1 t CO_2/TJ), and a net calorific value of 43.0 MJ/kg [48] with a density of 0.84 kg/L. EF_{grid} = 0.994 t CO_2e/MWh is the 2024 domestic-generation grid emission factor of South Africa published by the Department of Forestry, Fisheries and the Environment [49]. The factor is held constant over the 21-year horizon. As the South African generation mix shifts towards renewable and other low-carbon sources, the average grid factor over the project lifetime is likely to be lower, and ΔCO_2 in Equation (24) decreases in proportion to it; if EF_{grid} fell linearly to half of its 2024 value by the end of the project, the avoided emissions of the fully renewable configurations would be about 2740 t CO_2e instead of 3657 t (Section 3.5). Because EF_{grid} does not enter the optimisation, this affects only the reported avoided emissions, not the designs or their ranking. Avoided emissions are thus referred to the electricity actually delivered to the load, which is identical for all configurations; consequently, all configurations without a DG avoid exactly the same operational emissions. Emissions are priced at the South African carbon tax, introduced by the Carbon Tax Act [50], whose headline rate is ZAR 308 per tonne of CO_2e from 1 January 2026 [51], i.e., about US$18.5/t at an exchange rate of ZAR 16.6/US$. In the base case, the carbon cost is reported separately, and Section 3.13 internalises regulation-based carbon prices in the objective. To compare configurations on a life-cycle basis, the embodied emissions of PV (41 g CO_2e/kWh) and wind (11 g CO_2e/kWh) generation (IPCC AR5 medians [52], applied to all generated electricity, including curtailed output) and of battery manufacturing (83.5 kg CO_2e/kWh, the midpoint of 61–106 kg CO_2e/kWh [53], including one replacement) are added to the direct DG emissions and expressed per kWh delivered. Embodied emissions of the electrolyser, fuel cell and tank and the upstream emissions of diesel supply lie outside the system boundary (Section 4.5).

2.4.3. Renewable Energy Penetration Factor

The renewable energy penetration factor (REPF) is the share of renewable electricity in the electricity used by the system:

$$f_{ren} = 1 - \frac{E_{DG}}{E_{ren,used} + E_{DG}}, \quad (25)$$

where $E_{ren,used}$ (kWh) is the renewable electricity that is not curtailed and E_{DG} (kWh) is the DG output. Curtailment is reported separately as the share of available renewable output that is not used.

2.4.4. Employment Creation Factor

Employment is used as the social indicator, following the employment-factor approach commonly used to estimate energy-sector jobs [18]. The factors in Table 2 are expressed as average direct full-time-equivalent (FTE) jobs per MW of rated power (PV, wind, electrolyser, fuel cell, DG), per MWh of battery capacity and per kg of hydrogen-tank capacity, already combining annualised manufacturing and installation job-years with O&M jobs. For example, a 20 MW plant that employs 40 people in manufacturing for nine months and 25 people in installation for three months requires 1.8125 job-years/MW, which corresponds to 0.0725 FTE jobs/MW over a 25-year lifetime; with four full-time O&M staff (0.2 jobs/MW), the employment factor is 0.2725 FTE jobs/MW. The aggregate indicator and the cumulative employment are

$$ECF = \sum_c JC_c \frac{P_c}{1000}, \qquad J_{py} = N \cdot ECF, \quad (26)$$

where JC_c is the employment factor of component c (Table 2), P_c is its capacity in kW, kWh or kg (capacities in kW and kWh are converted to MW and MWh; for the hydrogen tank the divisor is 1), ECF (FTE jobs) is the average number of direct full-time jobs sustained over the project lifetime and J_{py} is the cumulative direct employment in person-years. The indicator covers direct jobs only and does not distinguish where they occur. Because PV modules, wind turbines, batteries, electrolysers and fuel cells are almost entirely imported into South Africa, ECF is also split ex post into local direct jobs (civil works, electrical installation and O&M), which remain in the community, and jobs embodied in equipment manufacturing, which are located largely abroad: $ECF_{loc} = \Sigma_c\, s_c\, JC_c\, P_c/1000$ and $ECF_{emb} = ECF - ECF_{loc}$, where s_c is the share of installation and O&M in the lifetime job-years of component c. For PV, wind turbines and the DG, s_c follows from the phase-resolved employment factors of [18] (construction and installation, manufacturing, and O&M over the 21-year lifetime; gas-fired generation for the DG): $s_{PV} = 0.80$, $s_{WT} = 0.67$ and $s_{DG} = 0.82$. Ref. [18] gives no phase-resolved factors for batteries and hydrogen equipment, which are manufactured abroad; their local share is therefore bounded by $s = 0$ (all jobs embodied in imported equipment) and an illustrative $s = 0.3$. The optimisation uses the total ECF of Equation (26); ECF_{loc} is evaluated for the reported designs (Section 3.6).

Table 2. Employment creation factors of the microgrid components, expressed as average direct FTE jobs per MW (per kg for the hydrogen tank and per MWh for the battery).

Component	Minimum	Mean	Maximum
Wind turbine conversion system	0.27	0.7	8.7
Solar PV modules	0.3	2.56	3.10
PEM-FC	0.747	0.808	0.880
PEM-EL	0	0.504	2
Pressure hydrogen storage tank	0	0.000008	0.2
Conventional diesel generator	0.15	0.156	0.18
Lithium-ion battery storage	0.02	0.72	2.086

2.4.5. Supply-Adequacy Indicators

Each design is simulated for all 10 years 2012–2021 with its capacities fixed and with unserved energy allowed at a penalty of US$1000/kWh, which is high enough that energy is left unserved only when the load cannot be met with the available capacities. The following adequacy indicators are reported [54]:

$$LPSP = \frac{\sum_t E_{ens}(t)}{\sum_t L(t)}, \tag{27}$$

$$h_{aut} = \frac{E_{use}}{\bar{L}}, \qquad h_{dis} = \frac{E_{use}}{\eta_{conv} P_{dis}},$$

where LPSP is the loss-of-power-supply probability (unserved-energy fraction), $E_{ens}(t)$ is the unserved energy, E_{use} is the usable AC-side storage energy ($0.95 M_{LPT} LHV \eta_{fc} \eta_{conv}$ for the HESS and $DoD\, E_{\max} \eta_D \eta_{conv}$ for the BESS), $\bar{L}$ is the mean load, h_{aut} is the storage autonomy in hours of mean load and h_{dis} is the discharge duration at rated discharge power P_{dis}. In addition, the number of hours with unserved energy, the longest outage, the longest renewable-deficit period (consecutive hours in which renewable output is below the load) and the firm-capacity margin at the annual peak are reported. Frequency and voltage dynamics and component failures are outside the scope of the hourly energy-balance model.

2.5. Multi-Objective Optimisation Model

The sizing problem is formulated as an MILP. The here-and-now decisions are the numbers of PV modules N_{pv} and wind turbines N_{wt} (integers), and the electrolyser, fuel-cell, converter, tank and battery ratings (continuous); the wait-and-see decisions are the hourly dispatch variables of Equations (7)–(18), which are re-optimised for every meteorological scenario. Three objectives are considered: TLC (economic), the direct GHG emissions of DG operation, GGE (environmental), and ECF (social).

A weighted sum of these objectives in their original units is dominated by the cost term (US$ 10^5–10^6 versus tonnes and fractions of a job), so that the result is essentially a least-cost design. Moreover, because ECF is linear in installed capacity, any normalised weighted sum that rewards ECF drives the components with the highest jobs:dollar ratio to their upper bounds, i.e., it rewards oversizing [55]. The multi-objective problem is therefore solved with the ε-constraint method [56], subject to the constraints of Equations (7)–(18):

$$\min_{x,y} TLC(x,y) \quad \text{s.t.} \quad GGE(y) \le \varepsilon_G, \quad ECF(x) \ge \varepsilon_J, \tag{28}$$

$$\tilde{f}_k = \frac{f_k - f_k^U}{f_k^N - f_k^U}, \tag{29}$$

$$x^* = \operatorname*{argmin}_{x \in \mathcal{D}} \sum_k w_k \tilde{f}_k, \qquad \sum_k w_k = 1,$$

where $\mathcal{D}$ is the set of Pareto-optimal designs generated for each configuration by tightening ε_J to +10%, +25%, +50% and +100% of the ECF of the least-cost design (+25% and +100% for the computationally more demanding DG-backed configurations) and, for the DG-backed configurations, ε_G to 50% and 10% of its emissions; and f_k^U and f_k^N are the best (utopia) and worst (nadir) values of objective k over $\mathcal{D}$ (ECF enters with a negative sign), so that each normalised objective $\tilde{f}_k$ lies in [0, 1]. The compromise design x^* for equal weights (1/3 each, or 1/2 each when GGE is identically zero) is reported as the reference design of each configuration. Because the normalisation is bounded by the Pareto set, the compromise cannot be pushed to arbitrary oversizing, and its sensitivity to the weights is examined by evaluating Equation (29) on a weight grid with a step of 0.05 (Section 3.7).

The model is implemented in Python 3.12 with SciPy 1.18.1 [57] and solved with the HiGHS solver (version 1.12.0, as bundled with SciPy 1.18.1; dual simplex and branch-and-cut) [58]. Configurations without a DG contain only two integer variables and are solved to a relative optimality gap of 0.1%. In the DG-backed configurations, the 8760 hourly commitment binaries make the joint problem intractable within practical time limits (in preliminary tests, a direct solution of Configuration C still had a relative gap of about 40% after 900 s). These configurations are therefore solved in two stages: stage 1 solves the problem with the commitment variables relaxed to $[0, 1]$, which yields the capacities and a valid lower bound on TLC; stage 2 fixes the capacities and solves the full unit-commitment MILP to a relative gap of 0.2%, which yields a feasible solution and the reported costs, fuel use and emissions. The difference between the two values is reported as an upper bound on the optimality gap of the design. The relaxation is weak in a known direction. With $X_g(t)$ relaxed, the cheapest commitment for a given output is $X_g(t) = P_g(t)/P_{g,r}$, so that the minimum load of 31% (Equation (15)) no longer binds, the no-load fuel term of Equation (14) becomes proportional to the output and the hour-based DG replacement and O&M costs are charged only on equivalent full-load hours. Stage 1 therefore treats the DG as a perfectly flexible unit and tends to cover small, frequent deficits with the DG rather than with storage, i.e., it undersizes storage and renewable capacity relative to the integer problem; the DG rating (51 kW) is fixed and is not affected. Part of the reported gap therefore reflects the weakness of the bound rather than a suboptimal design (Section 3.11). All computations were performed on a Linux machine with two virtual CPUs (Intel Xeon, 2.1 GHz; Intel Corporation, Santa Clara, CA, USA) and 7.6 GB of RAM; problem sizes, solution times and gaps are listed in Table A1 (Appendix A). For each configuration, the reported least-cost design is the design with the lowest TLC among all designs generated (the unconstrained run and the ε-constrained runs), because for the DG-backed configurations an ε-constrained run of the two-stage procedure can reach a lower cost than the unconstrained run.

2.6. Uncertainty Characterisation and Robust Optimisation

Uncertainty is considered in the economic, social and meteorological dimensions. Capital, replacement and fuel costs vary within $\pm\delta$ of their baseline values, where $\delta = 11\%, 21\%, 31\%$ and 41% defines the four uncertainty levels; the discount rate varies within the interval $[4.60\%, 24.98\%]$ (Table 3), and the employment factors vary between the minimum and maximum values in Table 2. These parameters form independent box (interval) uncertainty sets, Equation (30). For meteorological uncertainty, combining hourly extremes of irradiance and wind speed independently would produce sequences that never occur in reality (e.g., minimum irradiance and minimum wind in every hour of the year). The meteorological uncertainty set is therefore the set $\mathcal{S}$ of the 10 complete historical years 2012–2021, each represented by its full, temporally coherent 8760 h profile. The robust counterpart, in which x and y_s satisfy Equations (7)–(18) for all $s \in S_k$, is

$$c \in \left[(1-\delta)c^0, (1+\delta)c^0\right], \quad r \in \left[r^l, r^u\right], \tag{30}$$

$$JC_c \in [JC_c^{\min}, JC_c^{\max}], \quad s \in \mathcal{S},$$

$$\min_{x,\{y_s\}} \tau \quad \text{s.t.} \quad \tau \geq TLC\left(x, y_s; (1+\delta)c^0, r\right) \tag{31}$$

$$\forall s \in \mathcal{S}^k,\ r \in \left\{r^l, r^u\right\},$$

$$ECF\left(x; JC^{\min}\right) \geq \varepsilon_J^{rob}, \qquad GGE(y_s) \leq \varepsilon_G \ \ \forall s \in \mathcal{S}^k. \tag{32}$$

Table 3. Solar PV, wind turbine, meteorological, load and general project parameters.

Parameter	Value
Solar PV	
Rated power per module at STC (W)	351
Module efficiency at STC/module area (m^2)	19.04%/1.843
Temperature coefficient of maximum power (%/K)	−0.46
NOCT (K)/reference cell temperature (K)	319/298.15
Derating factor f_{pv}	0.85
Array tilt/azimuth/ground albedo	27°/north-facing/0.2
Wind turbine	
Rated power (kW)	51
Cut-in/rated/cut-out wind speed (m/s)	3.8/10/28
Hub height/reference height (m)/shear exponent	70/50/0.229
Meteorological data and load	
Data source/location	NASA POWER (CERES SYN1deg, MERRA-2)/27.18° S, 28.99° E
Years used/design year	2012–2021/2015
Annual GHI (kWh/m^2)	1983–2123
Annual specific PV yield (kWh/kWp)	1688–1777
Hub-height mean wind speed (m/s)/wind capacity factor	5.60–5.97/23.5–27.8%
Load: mean/peak (kW)/annual energy (MWh)	20.0/36.8/175.2
General project	
Project lifetime (years)	21
Discount rate (%)/uncertainty range (%)	9.26/4.60–24.98

Because TLC is non-decreasing in every cost coefficient for non-negative capacities and flows, the worst case of the cost box is attained at its upper bounds $(1 + \delta)c^0$ (a Soyster-type counterpart [59]); ECF is maximised and the capacities are non-negative, so its worst case is attained at the lower bounds of the employment factors. TLC is not monotonic in the discount rate, because a higher rate reduces the present value of future costs but also that of the salvage value; both interval endpoints are therefore included in the epigraph constraint (31). For all designs of this study, an evaluation on a grid of 60 discount rates showed that TLC decreases monotonically over the interval, so that the worst case is attained at its lower end. The capacities x are here-and-now decisions that must be feasible for every scenario, while the hourly dispatch y_s is a recourse decision for each year. The robust employment target ε_J^{rob} and the emission limit ε_G are those of the deterministic compromise design of the same configuration, evaluated with the worst-case factors.

Problems (31)–(32) are solved by constraint (scenario) generation [60]: starting from $\mathcal{S}^0 = \{\text{design year}\}$ (for the DG-backed configurations, the year with the highest fuel use in the back-test of the deterministic design is included from the start), the design is optimised, simulated for all 10 years with unserved energy allowed, and the year with the largest unserved energy (or, if no year has unserved energy, the year with the highest TLC) is added to $\mathcal{S}^k$. The procedure stops when the design serves the load in all 10 years and the worst-case TLC over all years does not exceed τ by more than 0.5%. The final back-test, with zero unserved energy in every historical year, is the feasibility certificate of each robust design. A temporally coherent budget of uncertainty (e.g., [61]) extends the analysis to conditions more extreme than those observed in 2012–2021 (Section 4.5).

2.7. Operational and Wear Constraints

The core formulation (Equations (7)–(18)) contains the DG unit commitment with minimum load, the state-of-charge and tank-pressure limits and the converter limits. To test whether the designs remain valid under a fuller description of operation and component

wear, an operational layer is added in which the following constraints become binding parts of the model. Battery power is limited by a C-rate $c_r = 0.5\ \mathrm{h}^{-1}$ (a minimum duration of 2 h), and the electrolyser and fuel cell have on/off states with a minimum stable load of 10% of rated power [62]:

$$P_C(t) \le c_r E_{\max}, \qquad P_D(t) + R_B(t) \le c_r E_{\max}, \tag{33}$$

$$\mu_{el} P_{el,r} X_{el}(t) \le P_{el}(t) \le P_{el,r} X_{el}(t), \qquad \mu_{fc} P_{fc,r} X_{fc}(t) \le P_{fc}(t) \le P_{fc,r} X_{fc}(t), \tag{34}$$

where $X_{el}(t), X_{fc}(t) \in \{0,1\}$ are the on/off states and $\mu_{el} = \mu_{fc} = 0.10$ are the minimum-load fractions. The DG must remain on or off for at least 2 h after each start-up or shut-down:

$$SU(t) - SD(t) = X_g(t) - X_g(t-1), \qquad \sum_{\tau=t-UT+1}^{t} SU(\tau) \le X_g(t), \qquad \sum_{\tau=t-DT+1}^{t} SD(\tau) \le 1 - X_g(t), \tag{35}$$

where $SU(t), SD(t) \in \{0,1\}$ are the start-up and shut-down indicators of the DG and $UT = DT = 2$ h are the minimum up and down times.

An operating reserve protects the supply against forecast errors and sudden drops in renewable output. Following standard practice for stand-alone systems [63], the reserve must cover 10% of the load, plus 25% of the PV output and 50% of the wind output, in every hour. Batteries and fuel cells provide fast reserve through the converter, limited by their power headroom and by the energy that can be sustained for one hour; the DG provides spinning reserve only when it is on:

$$\eta_{conv}(R_B(t) + R_{FC}(t)) + R_G(t) \ge 0.10L(t) + 0.25P_{pv}^{u}(t) + 0.50\left(P_{wt}^{L}(t) + P_{rec}(t)\right), \tag{36}$$

$$P_{inv}(t) + R_B(t) + R_{FC}(t) \le P_{conv}, \qquad R_G(t) + P_g(t) \le P_{g,r} X_g(t),$$

$$R_B(t) \le \eta_D(SoC(t) - (1 - DoD)E_{\max}), \qquad R_{FC}(t) + P_{fc}(t) \le P_{fc,r},$$

$$R_{FC}(t) \le (m(t) - 0.05M_{LPT})LHV\,\eta_{fc},$$

where $R_B(t)$, $R_{FC}(t)$ and $R_G(t)$ (kW) are the reserves provided by the battery, the fuel cell and the DG, respectively.

Component wear is represented by throughput- and hour-based replacement. A battery is replaced when either its calendar life (11 years) or its cycle life of 6000 equivalent full cycles at the usable depth of discharge is reached; vendor warranties of up to 10,000 cycles at 80% depth of discharge are reported for lithium iron phosphate systems [64], so the assumed cycle life is conservative. The PEM electrolyser stack is replaced after its calendar life (16 years) or after 60,000 operating hours at rated power, the lower end of the 50,000–80,000 h range reported for current PEM stacks [65]. The fuel cell and the DG retain their hour-based replacement (Section 2.4.1). The replacement cost of the battery and of the electrolyser is therefore

$$R_{bat}^{NPV} = \max\left\{R_{bat}^{cal}, \frac{R_{bat} k_{bat}}{N_{cyc}\, DoD} \sum_{n=1}^{N} \frac{\sum_t P_D(t)}{(1+r)^n}\right\}, \qquad R_{el}^{NPV} = \max\left\{R_{el}^{cal}, \frac{R_{el} k_{el}}{L_{el}^{h}} \sum_{n=1}^{N} \frac{\sum_t P_{el}(t)}{(1+r)^n}\right\}, \tag{37}$$

where R^{cal} is the calendar-based replacement cost of Equation (21), N_{cyc} is the cycle life and L_{el}^{h} is the stack lifetime in hours. Both maxima are written in epigraph form, so the model remains an MILP. The commitment binaries of the electrolyser and the fuel cell add 2×8760 binary variables per year. The operational models of Configurations A, B, C and E are therefore solved with the two-stage procedure of Section 2.5 (relaxed commitment for the capacities, weekly unit commitment of all units with fixed capacities). Where the weekly unit commitment cannot serve the load in some hours, that energy is added to the load of the first stage and the capacities are re-optimised, until the load is served; the gap between the two stages is reported. The operational layer is applied to the least-cost designs of all five configurations and to the back-tests of the compromise and robust designs over 2012–2021.

2.8. Input Parameters

Table 1 lists the cost assumptions for the system components. They are of the same order as the values used in recent techno-economic studies of hybrid hydrogen and battery systems [19,23,31,32].

The employment factors of the components (Table 2) vary widely, reflecting differences in technology maturity, supply-chain localisation and study scope. Wind turbine conversion systems show the widest range (0.27–8.7), followed by PV modules (0.3–3.10, mean 2.56). The PEM-FC factor is relatively consistent (0.747–0.880), whereas that of the PEM-EL varies between 0 and 2. The pressure hydrogen tank contributes little, as does the DG (0.15–0.18), while lithium-ion battery storage ranges from 0.02 to 2.086. The mean values are used in the deterministic optimisation, and the full ranges define the social uncertainty set used in the robust optimisation. All factors are expressed as average FTE jobs per unit of capacity (Section 2.4.4).

The PV modules have a rated output of 351 W at STC, an efficiency of 19.04% (module area 1.843 m^2) and a power temperature coefficient of −0.46%/K. The wind turbine has a rated output of 51 kW with cut-in, rated and cut-out wind speeds of 3.8, 10 and 28 m/s, respectively. The project lifetime is 21 years, and the baseline discount rate is 9.26% (Table 3).

The DG has a nominal output of 51 kW, a fuel-consumption slope of 0.274 L/kWh, a fuel-curve intercept of 0.034 L/h/kW and a minimum load ratio of 31%; the diesel price is \$2.29/L and the direct emission factor is 2.68 kg CO_2/L (Table 4).

Table 4. Diesel generator parameters.

Parameter	Value
Nominal power output (kW)	51
Fuel consumption slope (L/kWh)	0.274
Fuel curve intercept (L/h per kW rated)	0.034
Minimum load ratio (%)	31
Diesel fuel price (\$/L)	2.29
Direct CO_2 emission factor (kg/L) [48]	2.68
Permitted use	AC load only (no storage charging)

2.9. Scenario Analyses: Robustness, Carbon Pricing and Hydrogen Cost

Three sets of scenario analyses test how far the findings depend on the input data and on policy and technology assumptions. In each scenario, the least-cost design of every configuration is re-optimised with the deterministic model, so that capacities, dispatch and costs adapt to the changed inputs. For the DG-backed configurations, the base least-cost design re-dispatched under the changed inputs is evaluated as well, and the cheaper of the two designs is reported, which is the same rule as used for the base designs (Section 2.5).

Robustness of the findings. Four groups of instances are evaluated. (i) Design year: each of the 10 historical years 2012–2021 is used in turn as the design year. (ii) Use cases: the load is replaced by the DEL benchmark profiles of rural Free State households electrified for up to 15 years and of newly electrified informal-settlement households in Gauteng [40], which have sharper evening peaks (peak-to-mean ratios of 2.26 and 2.05 instead of 1.84), and by a mixed community load in which 30% of the annual demand is a productive daytime load (schools, clinics, water pumping or agro-processing) supplied on weekdays between 08:00 and 17:00. The annual demand is kept at 175.2 MWh in all use cases. (iii) Site archetypes: the hourly wind speeds are scaled by ±15% and the irradiance by ±10%, giving a windy but less sunny site, a sunny low-wind site and sites with jointly rich or poor resources; the shapes of the hourly series are preserved. (iv) Monte Carlo sampling: 6 joint samples are drawn of all component costs (±30%, independently uniform), the electrolyser efficiency (65–80%

HHV), the fuel-cell efficiency (45–60% LHV), the discount rate (4.6–15%), the diesel price (US$1.50–3.00/L), the annual demand (±20%) and the weather year (2012–2021); the rank of each configuration by lifetime cost is recorded for every sample.

Carbon pricing. Regulation-based carbon prices are internalised in the objective as a cost on direct DG emissions: the South African carbon tax of ZAR 308/t CO_2e in 2026 (about US$18.5/t) [51], the EU ETS allowance price of €88.3/t on 12 October 2026 (about US$99/t at US$1.117/€) [66] and the social cost of carbon of US$190/t estimated by the U.S. EPA [67]. The EU ETS level represents the price faced by emitters in a mature cap-and-trade market and, through the EU carbon border adjustment mechanism, by exporters of covered goods to the EU.

Hydrogen cost reduction. The investment and replacement costs of the electrolyser, fuel cell and tank are reduced by 25%, 50% and 75%. These steps span the reductions of 40% in the short term and up to 80% in the long term projected by IRENA for electrolysers [65]. A further scenario combines a 50% reduction of hydrogen equipment costs with a 40% reduction of battery costs, because battery costs are expected to fall in parallel.

3. Results

3.1. Optimal Designs Under Deterministic Optimisation

Table 5 summarises the least-cost and the equal-weight compromise designs of the five configurations for the design year. The least-cost designs rank as C < A < E < B < D in terms of total lifetime cost. Configuration B relies on three wind turbines, 73 kWp of PV and a hydrogen chain of 50 kW (electrolyser), 38 kW (fuel cell) and 160 kg (tank), whereas Configuration D requires 153 kWp of PV, two wind turbines and a 682 kWh battery. In the hybrid Configuration E, the optimiser combines a 254 kWh battery with a small hydrogen chain (8.3 kW electrolyser, 11.8 kW fuel cell) but a comparatively large tank of 101 kg: the electrolyser runs for many hours at low power to accumulate hydrogen, which the fuel cell returns during multi-day deficits. The DG-backed Configurations A and C need markedly smaller renewable and storage capacities (31 and 42 kWp of PV), because the 51 kW DG covers residual deficits. The converter rating of the fully renewable designs (38–47 kW) is set by the peak load supplied from the DC bus, divided by the converter efficiency.

Table 5. Optimal designs and key performance indicators under deterministic optimisation (design year 2015). Each cell gives the least-cost design/the equal-weight compromise design; a single value means that both coincide.

Item	A: RES–HESS–DG	B: RES–HESS	C: RES–BESS–DG	D: RES–BESS	E: RES–HESS–BESS
PV modules (number)	87/152	207/443	120/269	437/313	207/288
PV capacity (kWp)	30.5/53.4	72.7/155.5	42.1/94.4	153.4/109.9	72.7/101.1
Wind turbines (number)	2/3	3/2	2/1	2/1	2/1
Electrolyser (kW)	15.0/35.4	49.7/48.3	–	–	8.3/2.1
Fuel cell (kW)	6.0/22.5	38.3	–	–	11.8/8.8
Hydrogen tank (kg)	11.9/66.2	160.3/104.6	–	–	100.7/75.2
Battery (kWh)	–	–	196/346	682/1550	254/368
Converter rating (kW)	19.2/36.9	46.7/38.3	26.6/35.1	38.3	38.3
Diesel generator (kW)	51	–	51	–	–
Total lifetime cost (k$)	1258/1406	1707/1962	987/1128	1837/2057	1283/1304
$LCOE_{served}$ ($/kWh)	0.788/0.880	1.069/1.228	0.618/0.706	1.150/1.288	0.803/0.817
$LCOE_{gen}$ ($/kWh) [1]	0.177/0.150	0.174/0.188	0.146/0.190	0.177/0.321	0.173/0.214
Lifetime fuel cost, NPV (k$)	458.0/92.4	–	162.5/33.1	–	–
Renewable penetration (%)	70.3/95.2	100.0	88.1/97.7	100.0	100.0
Curtailment (% of available RES)	50.3/45.3	42.0/45.4	45.0/31.6	61.5/36.0	41.4/30.4

Table 5. *Cont.*

Item	A: RES–HESS–DG	B: RES–HESS	C: RES–BESS–DG	D: RES–BESS	E: RES–HESS–BESS
Direct DG CO_2 (t) [2]	1235/249	–	438/89	–	–
Carbon tax on DG emissions (k$) [2]	22.84/4.61	–	8.10/1.65	–	–
Avoided GHG vs. grid (t CO_2e) [2]	2422/3408	3657	3219/3568	3657	3657
Life-cycle intensity (g CO_2e/kWh)	362/111	51/78	159/86	108/122	55/65
Employment, ECF (FTE jobs)	0.170/0.288	0.350/0.526	0.328/0.535	0.955/1.433	0.455/0.568
Cumulative employment (person-years)	3.6/6.1	7.4/11.0	6.9/11.2	20.1/30.1	9.5/11.9

–, not applicable. [1] Lifetime cost divided by all generated electricity, including curtailed output; shown for comparison. [2] Cumulative over the 21-year project lifetime; carbon tax at US$18.5/t CO_2. All configurations deliver the same 175.2 MWh/yr to the load.

The compromise designs trade a moderate cost increase for higher employment and, in the DG-backed configurations, lower emissions: their TLC is 12% (A), 15% (B), 14% (C), 12% (D) and 2% (E) above the least-cost value. The choice of compromise is examined in Section 3.7; unless stated otherwise, the compromise designs are used as the reference designs in the following sections.

3.2. Economic Performance and the Choice of Cost Metric

The total lifetime cost of the compromise designs ranges from 1.13 M$ (C) to 2.06 M$ (D) (Figure 3a). In the fully renewable configurations, PV and wind account for 41–65% of TLC; storage accounts for 31% (B, hydrogen), 56% (D, battery) and 35% (E, hydrogen and battery); and in the DG-backed configurations, fuel and DG costs account for 10% (A) and 6% (C).

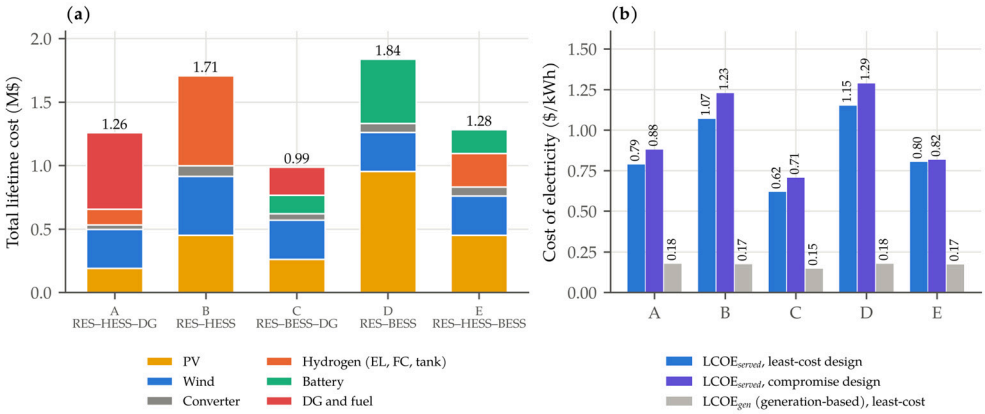


Figure 3. Economic performance under deterministic optimisation: (**a**) total lifetime cost of the least-cost designs by component; (**b**) levelised cost per kWh delivered to the load ($LCOE_{served}$) for the least-cost and compromise designs, compared with the cost per kWh generated ($LCOE_{gen}$).

Because all configurations deliver the same 175.2 MWh/yr, $LCOE_{served}$ follows the ranking of TLC exactly: C 0.71 $/kWh, E 0.82 $/kWh, A 0.88 $/kWh, B 1.23 $/kWh, D 1.29 $/kWh for the compromise designs (Figure 3b). The generation-based metric $LCOE_{gen}$ is only 0.15–0.32 $/kWh for the same designs, i.e., 4–7 times lower, because the fully renewable designs curtail a large share of their output (Section 3.3) and the curtailed energy inflates the denominator. $LCOE_{gen}$ also changes the ranking (A, B, C, E, D, from lowest to highest), whereas $LCOE_{served}$ ranks the designs as C, E, A, B, D. Because $LCOE_{gen}$ rewards curtailed output, all economic comparisons in this study use $LCOE_{served}$ or TLC.

The absolute values of $LCOE_{served}$ are high because the cost inputs of Table 1 include multipliers of 2.09–2.38 that raise, for example, the installed PV cost to 4.9 $/W, and because

a stand-alone system must be sized for the worst periods of the year. Without the multipliers, $LCOE_{served}$ of the least-cost designs falls to 0.31–0.50 $/kWh (Section 3.9).

3.3. Energy Balances, Curtailment and Storage Operation

Table 6 gives the complete annual energy balance of the compromise designs. In every configuration, the balance closes to within numerical precision, and the electricity delivered to the load is identical (175.2 MWh). The fully renewable designs generate 290–498 MWh/yr but curtail 30–45% of it (Figure 4). The curtailed energy is the least-cost (or compromise) response to the seasonal and multi-day variability of the resource, because additional PV or wind capacity is cheaper than additional storage for bridging the worst periods. The hydrogen chain loses 92 MWh/yr in Configuration B (69% of the electrolyser input), which is consistent with its electricity-to-electricity efficiency of 31%, whereas battery losses in Configuration D amount to 15 MWh/yr.

Table 6. Annual energy balance of the compromise designs in the design year (MWh/yr unless stated otherwise).

Item	A: RES–HESS–DG	B: RES–HESS	C: RES–BESS–DG	D: RES–BESS	E: RES–HESS–BESS
PV, available	93.1	271.3	164.7	191.7	176.4
Wind, available	339.9	226.6	113.3	113.3	113.3
Renewable output curtailed	196.3	225.8	87.8	109.8	88.1
Curtailment (% of available)	45.3	45.4	31.6	36.0	30.4
DG output	11.9	–	4.5	–	–
DG operating hours (h)	666	–	195	–	–
Electrolyser input	97.4	133.2	–	–	8.8
Fuel-cell output	30.1	41.1	–	–	2.7
Battery charge	–	–	69.5	71.0	72.3
Battery discharge	–	–	54.4	55.6	56.6
Storage losses	67.3	92.1	15.1	15.4	21.8
Converter flows (inverter + rectifier)	122.9	119.2	108.7	113.0	114.6
Converter losses	4.9	4.8	4.3	4.5	4.6
Dump load (DG minimum-load excess)	1.24	–	0.11	–	–
Electricity delivered to the load	175.2	175.2	175.2	175.2	175.2
Balance closure error	2.9×10^{-14}	5.8×10^{-14}	0	0	0

Closure error = |renewable output used + DG output − (load + storage losses + converter losses + dump load)|.

Figure 5 shows the hourly operation of the fully renewable compromise designs during the week with the largest renewable deficit of the design year (19–26 March 2015). In Configuration B, the fuel cell covers every evening and night peak, and the hydrogen tank is drawn down steadily over the week, from 99% to 35% of its capacity. In Configuration D, the 1550 kWh battery of the compromise design must also bridge the whole week, and its state of charge falls from 97% to 20%, i.e., the battery is used as multi-day storage, which is the expensive part of design D. In Configuration E, the battery cycles daily (mean daily swing 53% of capacity) while the hydrogen tank supplies the energy that is missing over several days (100% to 15%). The reference lines in the lower panels show that the battery of D reaches its minimum state of charge of 9% at the end of the week and that of E reaches it several times, whereas the hydrogen tanks remain above their 5% minimum (lowest levels about 30% in B and 15% in E). The longest renewable-deficit period of the design year lasts 19 h (B), 21 h (D) and 21 h (E) (Table 7).

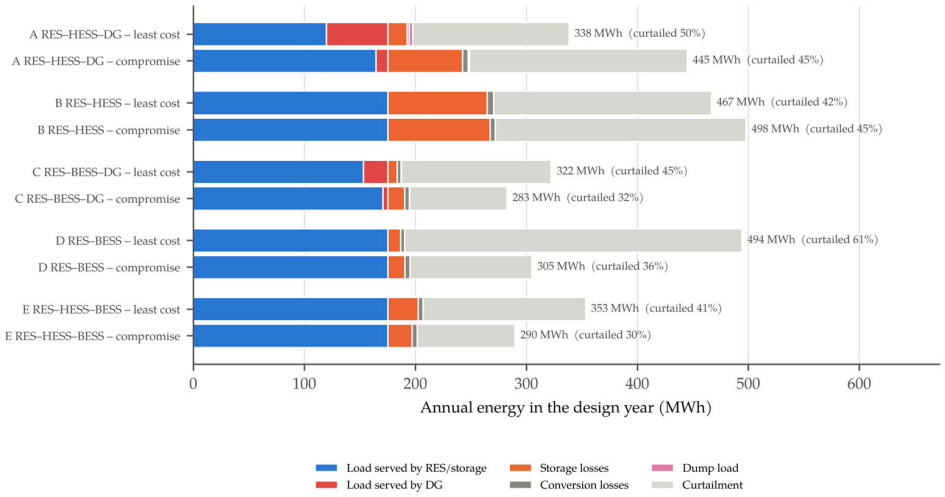


Figure 4. Use of the available renewable and diesel energy in the design year for the least-cost and compromise designs: electricity delivered to the load, storage and conversion losses, dump-load energy and curtailed renewable output.

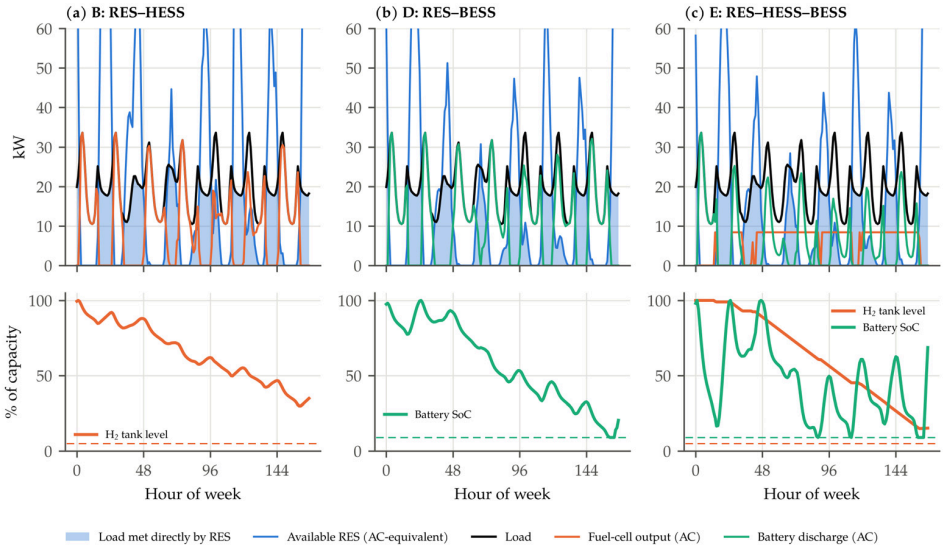


Figure 5. Hourly operation of the fully renewable compromise designs during the week with the largest renewable deficit of the design year (19–26 March 2015): load, available renewable power (AC-equivalent), load met directly by renewables, fuel-cell output and battery discharge (**upper panels**); storage level as a percentage of capacity (**lower panels**). Dashed lines in the lower panels mark the minimum hydrogen level of 5% of tank capacity (orange) and the minimum battery state of charge, 1 − DoD = 9% of capacity (green). In the **upper panels**, the black line is the load, the blue line the available renewable power (peaks above 60 kW are cut off), the light-blue area the load met directly by renewables, and the orange and green lines the fuel-cell output and the battery discharge, respectively.

Table 7. Storage operation and supply-adequacy indicators of the compromise designs (design year and back-test over 2012–2021 with fixed capacities).

Item	A: RES–HESS–DG	B: RES–HESS	C: RES–BESS–DG	D: RES–BESS	E: RES–HESS–BESS
Usable storage energy, AC side (kWh)	1006	1590	260	1164	1420
Storage autonomy at mean load (h)	50.3	79.5	13.0	58.2	71.0

Table 7. *Cont.*

Item	A: RES–HESS–DG	B: RES–HESS	C: RES–BESS–DG	D: RES–BESS	E: RES–HESS–BESS
Discharge duration at rated power (h)	46.6	43.2	0.8	0.8	3.9
Storage output to the DC bus (MWh/yr)	30.1	41.1	54.4	55.6	59.3
Longest renewable-deficit period, design year (h)	35	19	21	21	21
Firm-capacity margin at peak load (%)	97	0	130	0	0
Years with unserved energy (>1 kWh), 2012–2021	0	1	0	0	6
Maximum LPSP over 2012–2021 (%)	0.000	0.268	0.000	0.000	0.589
Maximum unserved energy in one year (MWh)	0.00	0.47	0.00	0.00	1.03
Maximum hours with unserved energy in one year	0	33	0	0	142
Longest outage (h)	0	12	0	0	14
Range of curtailment over 2012–2021 (%)	42–50	43–48	29–33	35–37	28–31

Usable storage energy and autonomy are defined in Equation (27); the firm-capacity margin counts the DG and the storage discharge capacity that can be delivered through the converter.

3.4. Storage Autonomy and Supply Adequacy

Table 7 quantifies the role of each storage technology. The usable hydrogen storage of Configuration B (1590 kWh) provides 79 h of autonomy at mean load and can be discharged at rated fuel-cell power for 43 h, whereas the battery of Configuration D provides 58 h of autonomy but only 0.8 h of discharge at its rated (1C) power. In Configuration E, the two are complementary: 71 h of autonomy are obtained with a battery that is 76% smaller than in D. The hydrogen tank in Configuration B completes about 25 equivalent full cycles per year and is used for multi-day balancing throughout the year. In Configuration E, the tank completes only about 2 equivalent full cycles per year: the small electrolyser fills it slowly over several weeks (about 4310 full-load hours per year), and it is drawn down mainly during the few prolonged deficits of the year, such as the one in late March shown in Figure 5. Hydrogen thus acts as a reserve for prolonged multi-day deficits; neither design shows a systematic seasonal (summer-to-winter) shift of energy.

When the compromise designs, which were optimised for 2015 only, are operated with fixed capacities in all 10 years 2012–2021, Configurations A, C and D serve the load in every year (LPSP = 0); Configuration B has unserved energy in 1 of the 10 years (maximum LPSP 0.27%, longest outage 12 h), Configuration E has unserved energy in 6 of the 10 years (maximum LPSP 0.59%, longest outage 14 h). The DG-backed designs are adequate by construction, because the DG alone exceeds the peak load (firm-capacity margin above 30%). For the fully renewable designs, these results show that a design sized for a single median year is not guaranteed to be adequate in drier or less windy years; the robust designs of Section 3.8 are therefore sized for all 10 years simultaneously and carry an explicit feasibility certificate. Component outages and frequency or voltage stability are not represented in the hourly energy-balance model; within this framework, the adequacy indicators quantify the resilience of supply to weather variability.

3.5. Environmental Performance

Relative to supply from the national grid (0.994 t CO_2e/MWh), every configuration that serves the same load without a DG avoids exactly the same operational emissions,

3657 t CO_2e over 21 years (Table 5). The DG-backed designs emit 249 t (A) and 89 t (C) of CO_2 over the project lifetime and therefore avoid 3408 t and 3568 t; the associated carbon tax is only 4.61 and 1.65 k$, respectively.

On a life-cycle basis, including the embodied emissions of PV, wind and battery manufacturing, the intensity of the delivered electricity is 111 (A), 78 (B), 86 (C), 122 (D) and 65 (E) g CO_2e/kWh, compared with about 820 g CO_2e/kWh for coal-fired generation [52]. The fully renewable configurations with large curtailment have a higher embodied footprint per delivered kWh, and battery manufacturing adds 259 t CO_2e in Configuration D. The system boundary covers PV, wind, and battery manufacturing and direct DG emissions; electrolyser, fuel-cell, and tank manufacturing and upstream diesel supply are outside it.

3.6. Employment Creation

With the factors of Table 2 expressed as average FTE jobs per unit of capacity, the compromise designs sustain 0.29 (A), 0.53 (B), 0.53 (C), 1.43 (D) and 0.57 (E) direct FTE jobs, i.e., 6, 11, 11, 30 and 12 person-years over the project lifetime (Table 5). Configuration D has the highest value. Battery capacity carries a high employment factor per dollar invested (0.72 FTE/MWh at about 0.75 M$/MWh including replacement), so the employment target of the battery-based compromise designs is met mainly by adding battery capacity, whereas PV accounts for most of the jobs in the other configurations. These figures are small because the microgrid is small (175 MWh/yr).

Under worst-case employment factors (the minimum values in Table 2), employment for the same designs falls to 0.08 (A), 0.10 (B), 0.06 (C), 0.08 (D), and 0.06 (E) FTE jobs. The decrease is largest for the battery-based designs because the battery factor ranges from 0.02 to 2.086 FTE/MWh (a ratio of 36 between the mean and the minimum), whereas the factors of wind turbines (ratio 2.6) and fuel cells (ratio 1.1) are less uncertain. Battery-based designs therefore show the largest reduction in employment under robust optimisation.

Splitting ECF into local and embodied jobs (Section 2.4.4) changes this picture. With storage-related jobs counted as fully embodied ($s = 0$; values for $s = 0.3$ in parentheses), the compromise designs sustain 0.19 (0.20) local FTE jobs in A, 0.37 (0.39) in B, 0.23 (0.30) in C, 0.25 (0.59) in D and 0.23 (0.31) in E. Local jobs thus account for 65–70% of ECF in the PV-based hydrogen designs A and B, but for only 17% (41%) in the battery-only design D, in which battery capacity provides 78% of ECF. For PV and wind, most job-years are in installation and O&M and therefore local, whereas the employment attributed to batteries and hydrogen equipment arises mainly in manufacturing abroad. At $s = 0$, the hydrogen-only design B sustains the most local jobs and D only the second most. Moreover, the compromise design of D, selected by raising ECF by 50%, sustains fewer local jobs than the least-cost design of D (0.25 versus 0.36 FTE at $s = 0$) at a 12% higher lifetime cost, because the additional jobs are embodied in imported battery capacity while PV capacity is reduced (at $s = 0.3$, the local gain is 14%). An objective based on total employment factors can therefore reward the purchase of imported capital assets rather than local employment; for community planning, ECF_{loc} should replace ECF in the ε-constraint of Equation (28), which the open model allows directly.

3.7. Multi-Objective Trade-Offs and Sensitivity to the Weights

Figure 6 shows the Pareto sets. Raising employment requires additional capacity at a nearly constant marginal cost of 949 k$ per additional FTE job (average slope between the least-cost design and the +100% point across configurations), i.e., about 45 k$ per person-year of direct employment. In the DG-backed configurations, reducing direct emissions is inexpensive at first and becomes increasingly costly as the system approaches full renewable supply (Figure 6b). With equal weights, the normalised compromise (Equation (29)) selects

A: emissions ≤ 10% of the least-cost design; B: ECF +50%; C: emissions ≤ 10% of the least-cost design; D: ECF +50%; E: ECF +25%.

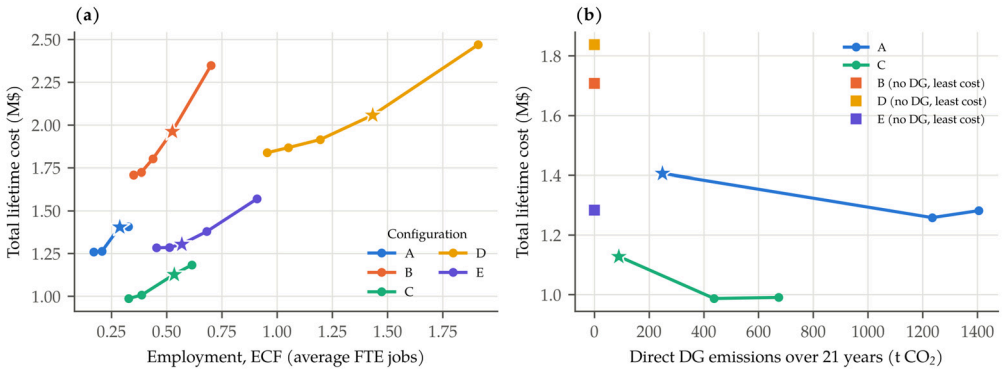


Figure 6. Pareto trade-offs: (**a**) lifetime cost versus employment for all configurations; (**b**) lifetime cost versus direct DG emissions for the DG-backed configurations, with the least-cost fully renewable designs shown for reference. Stars mark the equal-weight compromise designs. Letters A–E denote the five configurations (Section 2.1).

The compromise is sensitive to the weights, which is inherent to a weighted aggregation of objectives with very different units: over the weight grid, the equal-weight design is selected in 36% (A), 5% (B), 55% (C), 10% (D) and 14% (E) of the weight combinations, and the least-cost design in 3% (A), 19% (B), 19% (C), 33% (D) and 10% (E). Planners who attach little weight to employment would therefore choose the least-cost designs, whose results are also reported in Tables 5 and A1. The full Pareto sets and the weight-selection maps are provided in Table S1.

3.8. Robust Optimisation

Table 8 and Figure 7 report the robust designs. The constraint-generation procedure converged after at most 3 iterations (each level after the first started from the scenario set of the previous level); besides the design year, the final scenario sets contain 2013, 2017, 2019 and 2021. Every robust design serves the load in all 10 historical years (LPSP = 0), which is the feasibility certificate of the robust solutions. The worst-case TLC increases monotonically with the uncertainty level (A: 1.68–2.07 M$; B: 2.15–2.64 M$; C: 1.44–1.76 M$; D: 2.23–2.71 M$; E: 1.58–1.93 M$), because the worst case of the cost box is attained at its upper bound. For every design, the worst case over the discount-rate interval occurs at its lower end (4.6%), at which future O&M, replacement and fuel costs weigh most. At this rate the discounted delivered energy is also larger, so the worst-case $LCOE_{served}$ in Table 8 is lower than the deterministic values at 9.26% and should be compared only across uncertainty levels and configurations. Because capital, replacement and fuel costs are scaled by the same factor, the optimal capacities change only slightly between the levels (Table 8); the meteorological scenario set, which is the same at all levels, is what drives the differences between the robust and the deterministic designs. Consequently, quantities that depend only on the design and the weather, such as avoided emissions, are nearly constant across the levels, whereas the worst-case cost grows with δ. With $LCOE_{served}$, the worst-case cost per delivered kWh increases monotonically with δ for every configuration, and the ranking by cost (C < E < A < B < D) is the same at all levels.

Table 8. Robust designs and worst-case indicators at the four uncertainty levels.

Conf.	δ	Scenario Years	N_{pv}/N_{wt}	EL/FC/Tank (kW/kW/kg)	Battery (kWh)	Worst-Case TLC (k$)	Worst-Case $LCOE_{served}$ ($/kWh)	ECF at min. Factors (FTE)	DG CO_2, Worst Year (t)	Min. REPF (%)	Max. LPSP (%)
A	11%	2015, 2013	147/3	26/33/26	–	1678	0.721	0.089	339	92.9	0.000
	21%	2015, 2013	149/3	26/33/25	–	1807	0.776	0.089	336	93.0	0.000
	31%	2015, 2013	153/3	27/33/28	–	1939	0.833	0.089	314	93.5	0.000
	41%	2015, 2013	150/3	26/33/25	–	2066	0.888	0.089	342	92.8	0.000
B	11%	2015, 2017	220/4	41/38/151	–	2149	0.923	0.107	0	100.0	0.000
	21%	2015, 2017	227/4	42/38/137	–	2312	0.994	0.108	0	100.0	0.000
	31%	2015, 2017	228/4	42/38/135	–	2476	1.064	0.108	0	100.0	0.000
	41%	2015, 2017	228/4	42/38/135	–	2639	1.134	0.108	0	100.0	0.000
C	11%	2015, 2021	218/2	–	341	1441	0.619	0.065	119	97.2	0.000
	21%	2015, 2021	218/2	–	341	1547	0.665	0.065	119	97.2	0.000
	31%	2015, 2021	219/2	–	339	1653	0.710	0.065	119	97.2	0.000
	41%	2015, 2021	220/2	–	336	1759	0.756	0.065	119	97.2	0.000
D	11%	2015, 2019	437/2	–	682	2229	0.958	0.087	0	100.0	0.000
	21%	2015, 2019	437/2	–	682	2391	1.027	0.087	0	100.0	0.000
	31%	2015, 2019	437/2	–	682	2553	1.097	0.087	0	100.0	0.000
	41%	2015, 2019	437/2	–	682	2715	1.166	0.087	0	100.0	0.000
E	11%	2015, 2017, 2019	302/1	7/10/69	318	1580	0.679	0.059	0	100.0	0.000
	21%	2015, 2017, 2019	303/1	7/10/69	316	1698	0.729	0.059	0	100.0	0.000
	31%	2015, 2017, 2019	305/1	7/10/69	313	1815	0.780	0.059	0	100.0	0.000
	41%	2015, 2017, 2019	305/1	7/10/69	313	1932	0.830	0.059	0	100.0	0.000

Scenario years: historical years in the final scenario set $\mathcal{S}$ of the constraint-generation procedure (the first is the design year). Worst-case values are taken over the 10 back-test years and both ends of the discount-rate interval, with capital, replacement and fuel costs at $(1 + \delta)$ times their baseline; the worst case is attained at r = 4.6% in all cases, and the worst-case LCOE is evaluated at that rate. DG CO_2 is cumulative over 21 years for the year with the highest fuel use. Max. LPSP = 0 is the feasibility certificate of each robust design.

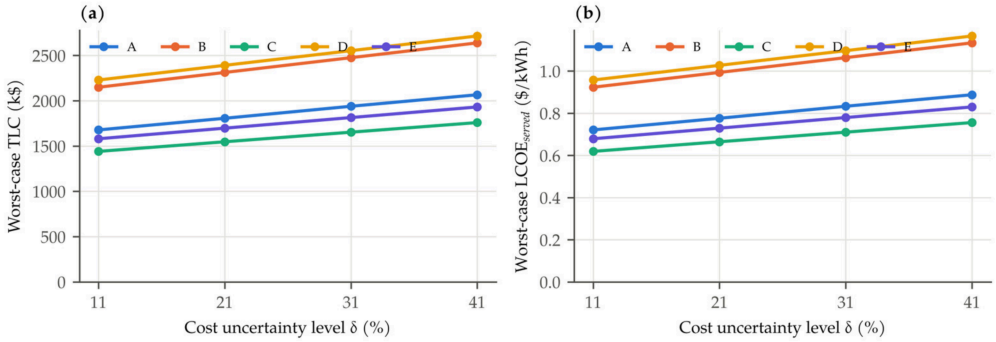


Figure 7. Robust optimisation results versus the cost uncertainty level: (**a**) worst-case total lifetime cost; (**b**) worst-case $LCOE_{served}$. Letters A–E denote the five configurations (Section 2.1).

3.9. Sensitivity Analyses

Figure 8 summarises the sensitivity analyses, in which the least-cost design was re-optimised for each case. Removing the cost multipliers (k = 1) reduces $LCOE_{served}$ by about 53%, to 0.31–0.50 $/kWh; the ranking changes from C < A < E < B < D to C < E < A < B < D, i.e., the fully renewable hybrid E becomes cheaper than the hydrogen–diesel configuration A. The efficiency of the hydrogen chain matters mainly for Configuration B: with a round-trip efficiency of 25%, $LCOE_{served}$ rises to 1.19 $/kWh, whereas an optimistic 52% would lower

it to 0.85 $/kWh. Configuration E is much less sensitive (0.72–0.83 $/kWh) because its battery handles most of the cycling. Scaling the load by ±30% changes $LCOE_{served}$ by less than 1%, because the model is nearly linear in the load apart from the integer numbers of PV modules and wind turbines. A PV derating factor of 0.75 instead of 0.85 increases $LCOE_{served}$ by 3–6%. A diesel factor of 3.7 kg/L that includes upstream supply, instead of the direct value of 2.68 kg/L, would increase the DG-related emissions of Configurations A and C by 38% but would not change any design, because emissions enter the optimisation only through the ε-constraints.

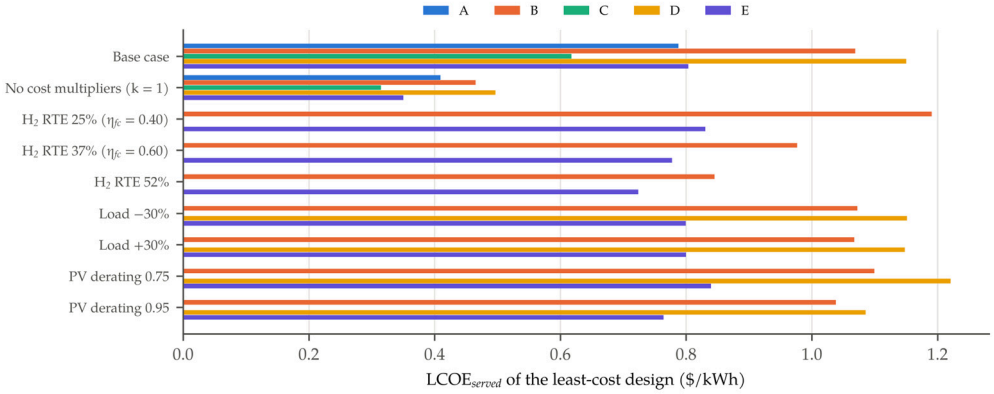


Figure 8. Sensitivity of $LCOE_{served}$ of the least-cost designs to the cost multipliers, the efficiency of the hydrogen chain, the load level and the PV derating factor (each case re-optimised; hydrogen-chain cases for Configurations B and E, load and PV cases for the fully renewable Configurations B, D and E). Letters A–E denote the five configurations (Section 2.1); H_2 RTE is the round-trip efficiency of the hydrogen chain (electricity to hydrogen to electricity), and *k* is the cost multiplier of Table 1.

3.10. Ranking of Configurations

Table 9 ranks the compromise designs by the key performance indicators. Configuration C ranks first for cost under both deterministic and robust optimisation, whereas the DG-backed Configurations A and C rank behind the fully renewable ones for renewable penetration and avoided emissions; the fully renewable configurations B, D and E share the first rank for avoided operational emissions and renewable penetration, and among them E is the least expensive. No configuration dominates on all criteria; the hydrogen-only design B ranks first for avoided emissions and renewable penetration, together with D and E, but not for any economic indicator.

Table 9. Ranking of the configurations (compromise designs) under deterministic optimisation and robust optimisation at the 41% uncertainty level.

KPI	A (Det.)	B (Det.)	C (Det.)	D (Det.)	E (Det.)	A (Rob.)	B (Rob.)	C (Rob.)	D (Rob.)	E (Rob.)
TLC and LCOE (served)	3rd	4th	1st	5th	2nd	3rd	4th	1st	5th	2nd
Avoided GHG emissions	5th	1st	4th	1st	1st	5th	1st	4th	1st	1st
Life-cycle GHG intensity	4th	2nd	3rd	5th	1st	–	–	–	–	–
Employment (ECF)	5th	4th	3rd	1st	2nd	2nd	1st	4th	3rd	5th
Renewable penetration	5th	1st	4th	1st	1st	5th	1st	4th	1st	1st
Curtailment (lower is better)	4th	5th	2nd	3rd	1st	–	–	–	–	–

Det., deterministic optimisation; Rob., robust optimisation at δ = 41% (worst-case values). Ties share the same rank. Rankings by TLC and by $LCOE_{served}$ are identical because all configurations deliver the same electricity.

3.11. Effect of Operational and Wear Constraints

Table 10 compares the least-cost designs obtained with the operational and wear layer of Section 2.7 with those of the core model. The additional constraints raise the lifetime cost by 0.8–8.8% (A +8.8%, B +3.9%, C +2.9%, D +0.8%, E +0.9%). The ranking becomes C < E < A < B < D; compared with the core model (C < A < E < B < D), the hydrogen–diesel configuration A and the fully renewable hybrid E, whose costs differ by less than 2% in the core model, change places, while the battery–diesel configuration C remains the least-cost option and E the least-cost fully renewable option. The fully renewable designs change little: the converter ratings of D and E grow by 3.8 kW each to carry the reserve through the inverter, and B adds 3 PV modules and 4.7 kg of tank capacity to compensate for the hydrogen that the electrolyser cannot produce below its minimum load. The DG-backed designs change more: A replaces part of its electrolyser and tank with a larger fuel cell (16.3 instead of 6.0 kW), which supplies fast reserve so that the DG need not run as spinning reserve, and C installs 24 fewer PV modules and a 28 kWh smaller battery while running its DG for 1535 h per year.

Table 10. Least-cost designs with the operational and wear layer (Section 2.7) compared with the core model (design year 2015), and 10-year back-tests of the compromise and robust designs with the operational layer.

Item	A: RES–HESS–DG	B: RES–HESS	C: RES–BESS–DG	D: RES–BESS	E: RES–HESS–BESS
TLC, core model (k$)	1258	1707	987	1837	1283
TLC, operational layer (k$)	1369	1773	1015	1852	1295
Change of TLC (%)	+8.8	+3.9	+2.9	+0.8	+0.9
$LCOE_{served}$, operational layer ($/kWh)	0.857	1.110	0.636	1.160	0.811
PV capacity (kWp), core → operational	31 → 29	73 → 74	42 → 34	153 → 153	73 → 73
Wind turbines (number)	2 → 2	3 → 3	2 → 2	2 → 2	2 → 2
Battery (kWh)	–	–	196 → 168	682 → 695	254 → 255
Electrolyser/fuel cell (kW), operational layer	12.2/16.3	53.2/42.2	–	–	8.2/11.8
Hydrogen tank (kg), core → operational	12 → 8	160 → 165	–	–	101 → 101
Converter (kW), core → operational	19.2 → 23.1	46.7 → 44.6	26.6 → 26.9	38.3 → 42.2	38.3 → 42.2
Battery equivalent full cycles per year	–	–	191	69	191
Battery replacement governed by	–	–	calendar	calendar	calendar
Electrolyser operating hours/starts per year	4670/872	4104/552	–	–	2841/203
Fuel-cell operating hours/starts per year	1658/625	2656/440	–	–	731/146
DG operating hours/starts per year	3643/626	–	1535/411	–	–
Hours with binding operating reserve	3135	1570	2587	2515	1557
Hours at electrolyser/fuel-cell minimum load	81/118	35/321	–	–	16/7
Hours with binding battery C-rate	–	–	0	0	0
Unserved energy in the design year (kWh)	0.1	1.2	0.0	0.0	0.3
Gap between the two stages (%)	29.5	1.8	14.7	0.0	0.2
Max. LPSP 2012–2021, compromise design (%)	0.000	0.289	0.000	0.000	0.589
Max. LPSP 2012–2021, robust design $\delta = 41\%$ (%)	0.000	0.035	0.000	0.000	0.000

–, not applicable. Operating statistics refer to the design year. The back-tests simulate each fixed design for 2012–2021 with weekly unit commitment of all units and the operating reserve of Equation (36).

The operating reserve is the constraint with the largest effect. It binds in 1557–3135 h of the design year, mostly in daytime hours, when the reserve for PV output adds to the load-related reserve; in the hydrogen-based configurations the inverter headroom is usually the limiting element, which explains the larger converter ratings. In the DG-backed configurations, the reserve also keeps the DG online at part load (A: 2431 h per year at minimum load; C: 411 DG starts per year, each followed by at least 2 h of operation). The minimum stable loads of the electrolyser and the fuel cell bind in 356 h of B and in 23 h of E, where the battery absorbs small surpluses and covers small deficits. The battery C-rate of 0.5 h^{-1} never binds, because the least-cost batteries discharge at well below their rated power, and the battery replacement remains calendar-governed (69 and 191 equivalent full cycles per year in D and E, compared with 6000 cycles over the 11-year calendar life). The electrolyser of B operates for 4104 h per year, equivalent to 2474 full-load hours, so its stack life of 60,000 h at rated power is not reached within its 16-year calendar life either. The unserved energy of the operational designs is at most 1.2 kWh per year (LPSP below 0.0007%), i.e., the operational designs fully supply the load.

The 10-year back-tests with the operational layer (last rows of Table 10) show how the designs of Sections 3.4 and 3.8 perform under unit commitment, minimum loads and the operating reserve. For the compromise designs the largest annual LPSP over 2012–2021 is 0.00% (A), 0.29% (B), 0.00% (C), 0.00% (D) and 0.59% (E), which differs from the core back-test (Table 7) by at most 0.02 percentage points: the years with unserved energy are the same, and the shortfalls are caused by the prolonged renewable deficits of those years rather than by the operational constraints. The robust designs at $\delta = 41\%$ reach a largest annual LPSP of 0.000% (A), 0.035% (B), 0.000% (C), 0.000% (D) and 0.000% (E) with the operational layer. B leaves at most 61 kWh per year unserved, because the minimum loads of the hydrogen chain reduce the hydrogen that can be produced from small surpluses. In the back-tests, the operating reserve is fully provided in all but 373 h per year.

The gaps between the two stages are largest for the DG-backed configurations (Table 10: 29.5% for A and 14.7% for C with the operational layer; Table A1: 22.7% and 5.9% for the least-cost and 4.0% and 1.1% for the compromise designs of the core model). Three observations show how they should be read. First, much of each gap stems from the weakness of the stage-1 bound (Section 2.5) rather than from the design. Evaluating the stage-2 dispatch of the compromise designs with the relaxed cost terms (no-load fuel proportional to output and hour-based DG costs on equivalent full-load hours) lowers their lifetime cost by 30.7 k$ (A, 2.2%) and 7.6 k$ (C, 0.7%), i.e., by about half of the gap of A and 60% of that of C. With the operational layer, the relaxation also allows the DG to provide spinning reserve at fractional commitment, whereas in stage 2, it must run at no less than 31% load to do so (A: 2431 h per year at minimum load), which explains the larger gaps of this layer. Second, the gaps grow with the reliance on the DG—they are largest for the least-cost design of A, whose DG supplies 30% of the energy used—consistent with the tendency of stage 1 to undersize storage. Third, because the reported costs of A and C are those of feasible designs, they are upper bounds; the bias can make the DG-backed configurations appear more expensive, but not cheaper, than they are. The bounds therefore certify that C is cheaper than every fully renewable configuration (its feasible cost lies below their lower bounds in both models) and, in the core model, that A is cheaper than E (1258 versus at least 1282 k$). They do not certify the order of A and C (lower bound of A 972 k$ versus 987 k$ for C in the core model) or, with the operational layer, the order of A and E; C was, however, the least-cost configuration in all 10 design years and all six Monte Carlo samples (Section 3.12). Tighter bounds would require a stronger stage-1 formulation, e.g., a lower bound on the DG operating hours derived from its minimum load, or longer branch-and-cut runs. The

wear model counts operating hours and throughput but not start–stop cycles. The effect of the frequent starts of the hydrogen chain in Table 10 is assessed in Section 4.5.

3.12. Robustness of the Findings

Figure 9 summarises the re-optimised least-cost designs for the instances, use cases, site archetypes and Monte Carlo samples of Section 2.9. Across the 10 design years, $LCOE_{served}$ lies within 0.76–0.80 $/kWh (A), 0.93–1.12 $/kWh (B), 0.60–0.62 $/kWh (C), 0.89–1.15 $/kWh (D) and 0.73–0.81 $/kWh (E). The battery–diesel configuration C is the least-cost option in 10 of 10 design years, and the hybrid E is the least-cost fully renewable option in 10 of 10 years. The order of the other configurations depends on the weather year: the hydrogen-only B is cheaper than the battery-only D in 3 of 10 years, and E is cheaper than the hydrogen–diesel A in 5 of 10 years, because the costs of A and E differ by only a few per cent.

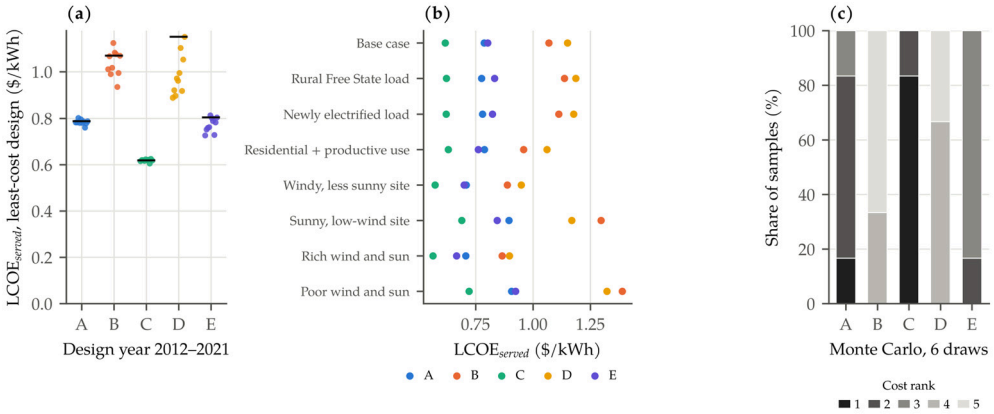


Figure 9. Robustness of the findings (least-cost designs, re-optimised for each case): (**a**) $LCOE_{served}$ for each design year 2012–2021 (horizontal bar: design year 2015); (**b**) $LCOE_{served}$ for the use cases and site archetypes; (**c**) rank of each configuration by lifetime cost in the Monte Carlo sample. Letters A–E denote the five configurations (Section 2.1); in (**c**), the numbers 1–5 give the rank of each configuration by lifetime cost (1 = lowest cost), and the shares refer to the six Monte Carlo draws.

The use cases and site archetypes change the absolute costs more than the design year does: $LCOE_{served}$ ranges from 0.62–0.63 $/kWh (C) to 0.76–0.83 $/kWh (E) across the use cases and from 0.56–0.72 $/kWh (C) to 0.67–0.92 $/kWh (E) across the site archetypes. The loads with sharper evening peaks raise $LCOE_{served}$ of the fully renewable designs by up to 6%, whereas the productive daytime load, which is supplied directly by PV, lowers it by up to 10%; the DG-backed designs change by less than 3%. In 7 of 7 cases C remains the least-cost configuration and in 7 of 7 cases E remains the least-cost fully renewable configuration (rural Free State households: C < A < E < B < D; newly electrified households: C < A < E < B < D; residential load with productive daytime use: C < E < A < B < D; windy, less sunny site: C < E < A < B < D; sunny, low-wind site: C < E < A < D < B; site with rich wind and solar resources: C < E < A < B < D; site with poor wind and solar resources: C < A < E < D < B).

In the Monte Carlo sample of six joint draws of all key inputs, C ranks first in six draws, and E is the least-cost fully renewable configuration in six draws; B is cheaper than D in two draws. In one draw with high discount rates, the least-cost designs of A and C both reduce to a PV/wind–DG system without storage and therefore cost the same. The principal findings, namely the least-cost role of a battery with a small DG backup at current costs and the advantage of combining hydrogen and battery storage in a fully renewable microgrid, are therefore robust to the design year, the load profile, the resource quality and

joint changes of the cost and efficiency parameters, whereas the comparison between the two single-storage configurations is not.

3.13. Carbon Pricing and Hydrogen Cost Reduction

Figure 10a shows the lifetime cost of the DG-backed configurations when regulation-based carbon prices are internalised in the objective. At the South African carbon tax of 2026 (US$18.5/t), the carbon cost adds 0.8% (A) and 0.4% (C) to the lifetime cost and leaves both designs unchanged. At the EU ETS price (US$99/t) and at the social cost of carbon (US$190/t), the lifetime cost of C rises by 1.5% and 3.5%, and that of A by 3.9% and 7.1%; the re-optimised designs keep the DG as backup, which supplies 12% (C) and 30% (A) of the delivered energy. The ranking changes in one respect: the fully renewable hybrid E (US$1.28 million) becomes cheaper than the hydrogen–diesel configuration A at carbon prices above about US$50/t, i.e., below the current EU ETS price. The battery–diesel configuration C remains the least-cost option at all three price levels; the carbon price at which E reaches the cost of C is of the order of US$1400–1600/t, an order of magnitude above current allowance prices, because C emits only 21 t CO_2 per year.

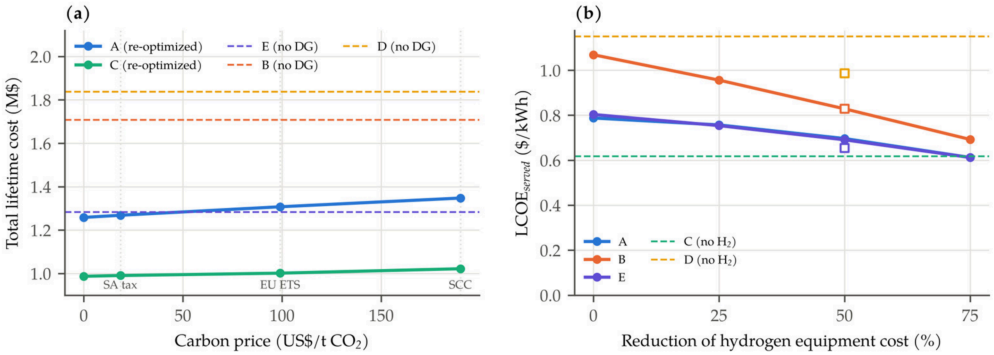


Figure 10. Policy and technology scenarios (least-cost designs, re-optimised): (**a**) total lifetime cost of the DG-backed configurations A and C versus the carbon price internalised in the objective (South African carbon tax 2026, EU ETS price of October 2026 and U.S. EPA social cost of carbon), with the costs of the fully renewable configurations for reference; (**b**) $LCOE_{served}$ versus the reduction of hydrogen equipment costs (open squares: hydrogen −50% combined with battery −40%). Letters A–E denote the five configurations (Section 2.1). In (**a**), SA tax, EU ETS and SCC mark the South African carbon tax, the EU ETS price and the U.S. EPA social cost of carbon; 'no DG' and 'no H_2' mark the configurations without a diesel generator or without hydrogen storage, shown for reference.

Lower hydrogen equipment costs change the results more strongly (Figure 10b). With costs reduced by 25%, 50% and 75%, $LCOE_{served}$ of the hydrogen-only configuration B falls from 1.07 to 0.96, 0.83 and 0.69 $/kWh, and that of the hybrid E from 0.80 to 0.75, 0.69 and 0.61 $/kWh, respectively. The optimiser shifts storage from the battery to hydrogen: in E the tank grows from 101 to 136, 156 and 263 kg while the battery shrinks from 254 to 206, 196 and 144 kWh, respectively. At a 75% reduction, close to the long-term reduction of up to 80% projected by IRENA, the fully renewable hybrid E (0.612 $/kWh) and the hydrogen–diesel A (0.612 $/kWh) reach the cost of the battery–diesel design C (0.618 $/kWh), so that a diesel-free microgrid becomes cost-competitive without a carbon price. When battery costs fall by 40% at the same time as hydrogen costs fall by 50%, E (0.654 $/kWh) remains cheaper than the battery-only D (0.987 $/kWh) and the hydrogen-only B (0.829 $/kWh), which confirms that the complementarity of the two storage technologies does not depend on a particular cost ratio.

4. Discussion

4.1. Complementary Roles of Hydrogen and Battery Storage

The results show a clear division of roles between the two storage technologies. Batteries, with a round-trip efficiency of about 78%, provide low-cost daily balancing and are the storage of choice when a DG covers the residual deficits (Configuration C). Hydrogen, with an electricity-to-electricity efficiency of only 31%, is valuable where energy must be stored for several days. In the fully renewable Configuration B, the tank provides 79 h of autonomy, and in the hybrid Configuration E, a small electrolyser and fuel cell combined with a 75 kg tank complement a battery and reduce the lifetime cost by 37% relative to the battery-only design D and by 34% relative to the hydrogen-only design B. Co-optimising both technologies under identical demand and adequacy constraints therefore confirms their complementarity directly rather than by inference. These findings are consistent with studies showing that hydrogen storage can mitigate the variability of wind and solar generation [33] and enable high or full renewable self-sufficiency [31,32].

Three further points characterise these results. First, the hydrogen tanks of the optimised designs (66 (A), 105 (B) and 75 (E) kg) store a few days of demand; they are used either for frequent multi-day balancing (B) or as a slowly replenished reserve for the few prolonged deficits of the year (E), but not for a systematic seasonal shift of energy. Second, adequacy is assessed for historical weather in 2012–2021 with perfect foresight of the hourly dispatch within each year; the operating reserve of Section 3.11 provides the margin that forecast-based dispatch requires. Third, resilience is quantified here as energy adequacy under 10 years of observed weather variability (LPSP, autonomy, longest deficit bridged) and as independence from diesel supply; frequency and voltage dynamics, component failures and black-start operation are addressed by dynamic models and are outside the scope of this planning study.

4.2. Economic Competitiveness in Context

Table 11 compares the cost of electricity obtained here with recent studies of stand-alone systems with hydrogen and/or battery storage. Published values for renewable systems with storage range from 0.10 $/kWh for a large PV–wind–battery system with an excellent resource at NEOM [68] to 0.83–1.02 $/kWh for a wind/PV–hydrogen island system [69], and diesel-only supply costs 0.67–1.04 $/kWh (or €/kWh) [70,71]. With the listed equipment prices (k = 1), the least-cost designs of this study cost 0.31–0.50 $/kWh, within the published range and close to the PV–hydrogen and PV–battery values of 0.51 and 0.58 $/kWh reported in [72]; with the installed-cost multipliers of Table 1, they cost 0.62–1.15 $/kWh, at the upper end of the range and close to the hydrogen-based island system of [69]. The diesel-only reference of this study (1.07 $/kWh at US$2.29/L) lies slightly above the published diesel costs, consistent with its higher fuel price.

The ranking of the storage options agrees with the literature where the studies are comparable. The combination of hydrogen and battery storage is the least-cost fully renewable option, as in the PV–battery–hydrogen microgrid of [70]; hydrogen-only storage is cheaper than battery-only storage in the design year, as reported for an off-grid PV system in [72], whereas a PV/wind–battery system was slightly cheaper than the same system with added hydrogen storage at NEOM [68]. Section 3.12 shows that the order of the two single-storage configurations depends on the weather year at the case-study site, while the advantage of the hybrid holds in all years. Part of the spread between studies is methodological: costs normalised by generated electricity, as is common in parts of the literature, are lower by a factor of 4–7 for fully renewable stand-alone systems with large curtailment, so comparisons between studies should state the denominator explicitly. The high capital cost of PV and storage in Table 1 (including the multipliers) is the main economic barrier; at the listed

equipment prices, the $LCOE_{served}$ of the fully renewable hybrid E falls to 0.35 $/kWh, below that of the hydrogen–diesel configuration A (0.41 $/kWh) and close to the battery–diesel configuration C (0.31 $/kWh), and Section 3.13 shows that hydrogen cost reductions of the magnitude projected for the coming decades make E cost-competitive with C.

Table 11. Cost of electricity of stand-alone renewable systems with hydrogen and/or battery storage reported in recent studies and obtained in this study (least-cost designs, LCOE per kWh served).

Study	Location and Scale	System (Storage)	Reported Cost of Electricity
Kalinci et al. [69]	Bozcaada island, Turkey	Wind/PV with EL–tank–FC	0.83–1.02 $/kWh
Madziga et al. [73]	Gwakwani village, South Africa; 6.6 kWh/day	PV–battery; PV–diesel	0.87; 0.78 $/kWh
Dawood et al. [70]	Remote community, Western Australia; 2 MWh/day	PV–battery; diesel only; PV–battery–hydrogen	0.39; 0.67 $/kWh; lowest of the three
Trapani et al. [71]	Remote islands, Norway	RES with hydrogen–battery; diesel only	0.21–0.63; 0.87–1.04 €/kWh
Shahverdian et al. [72]	Off-grid PV system	PV–hydrogen; PV–battery	0.51; 0.58 $/kWh
Alharbi et al. [68]	NEOM, Saudi Arabia; 2.4 MWh/day	PV/WT–battery; PV/WT–battery–hydrogen	0.097; 0.106 $/kWh
This study, cost multipliers k = 2.38/2.09	Highveld, South Africa; 0.48 MWh/day	C; A; E; B; D; diesel only	0.62; 0.79; 0.80; 1.07; 1.15; 1.07 $/kWh
This study, equipment prices (k = 1)	Highveld, South Africa; 0.48 MWh/day	C; A; E; B; D; diesel only	0.31; 0.41; 0.35; 0.47; 0.50; 1.01 $/kWh

Values are taken from the cited studies as reported (costs per kWh delivered to the load). Configurations of this study: C, RES–BESS–DG; A, RES–HESS–DG; E, RES–HESS–BESS; B, RES–HESS; D, RES–BESS; diesel only, the 51 kW DG supplying the load alone at US$2.29/L.

4.3. Implications for Sustainability

Environmental dimension. The fully renewable configurations eliminate direct diesel emissions and the associated carbon-tax liability and avoid 3657 t CO_2e of grid emissions over the project lifetime. On a life-cycle basis, the intensity of the delivered electricity remains an order of magnitude below that of coal-fired supply, although curtailment and battery manufacturing increase the embodied footprint per delivered kWh. Embodied emissions of electrolysers, fuel cells and tanks and the upstream emissions of diesel lie outside the system boundary and can be added in a full life-cycle assessment.

Social dimension. The employment results show that direct jobs scale with installed capacity: the compromise designs sustain 0.3–1.4 FTE jobs, of which 0.19–0.37 FTE (0.20–0.59 FTE if 30% of the storage-related jobs are local) are local installation and O&M jobs (Section 3.6). The local employment benefit of a single microgrid is therefore small; it becomes significant only when many systems are deployed and when installation and O&M capacity is built locally. Because batteries and hydrogen equipment are imported, a job indicator based on total employment factors favours capital-intensive imported storage; local job indicators, such as $ECF_{loc,}$ are better suited to rural development planning. Together, these outcomes relate the study to Sustainable Development Goals (SDGs) 7 (affordable and clean energy), 8 (decent work and economic growth) and 13 (climate action). Workforce training, local-content requirements and renewable subsidies could further increase the local share of the employment benefits and support a just transition [36].

Use of surplus energy. The curtailed renewable output of 88–226 MWh/yr in the fully renewable designs represents both an inefficiency and an opportunity. Using the surplus for flexible community services, such as water pumping, desalination, space heating or cooling, or for producing hydrogen for other uses, could improve the economics of the system and, in South Africa, reduce reliance on centralised supply during load shedding. Hydrogen produced from surplus electricity could in principle supply fuel-cell vehicles [11], low-carbon industrial feedstock [4] or heat. A scoping calculation indicates the size of this

lever. If a controllable load, such as water pumping into a reservoir or a cold store, absorbed a share φ of the curtailed output of the compromise designs without additional generation or storage capacity, the cost per kWh of useful energy (load plus absorbed surplus) would fall from $LCOE_{served}$ to $LCOE_{served} \cdot E_{served}/(E_{served} + \varphi E_{curt})$: for φ = 25%, from 1.23 to 0.93 $/kWh (B), from 1.29 to 1.11 $/kWh (D) and from 0.82 to 0.73 $/kWh (E), and for φ = 50%, to 0.75, 0.98 and 0.65 $/kWh, respectively. A quarter of the curtailed output of E (22 MWh/yr) would, for example, lift about 80,000 m^3 of water per year over a head of 50 m at a wire-to-water efficiency of 50%. The achievable φ depends on how well the surplus hours match the operating window and rating of the flexible load, on the converter and pump capacity and on the cost of the additional equipment; because these factors were not modelled, the figures indicate the potential rather than an optimised result. Co-optimising such flexible loads and other cross-sectoral uses with the microgrid is an avenue for future work.

4.4. Policy and Practical Implications

Several policy implications follow. First, because capital cost is the main barrier to fully renewable hydrogen-based microgrids, measures that accelerate cost reductions in electrolysers, fuel cells and advanced batteries—such as targeted subsidies, concessional and climate finance, and support for local manufacturing—would directly improve their competitiveness [74,75]. Second, carbon pricing should reflect the cost of emissions: at the carbon tax assumed here, the carbon-tax liability of the DG-backed systems (US$1649–4607 over 21 years) is negligible compared with their lifetime cost (US$1.13–1.41 million), so the carbon price alone provides only a weak incentive to move away from diesel backup; fiscal instruments therefore need to be designed together with other support measures [76]. Third, renewable portfolio standards, supportive regulation for microgrids and clear safety and infrastructure standards for hydrogen would reduce investment risk [14,77]. Fourth, cross-sectoral planning that links microgrid hydrogen production with transport, heating and industry could create additional revenue streams [78]. Finally, workforce training and local-content policies can increase employment benefits and make the energy transition more inclusive [36].

The scenario analysis of Section 3.13 quantifies the levers available to policy makers. A carbon price above about US$50/t, i.e., below the current EU ETS price of about US$99/t, is sufficient to make the diesel-free hybrid E cheaper than the hydrogen–diesel configuration A, whereas replacing a battery–diesel system, such as C, would require a carbon price of the order of US$1400–1600/t. Reducing the cost of hydrogen equipment by about 75%, in line with long-term projections [65], achieves the same result without a carbon price. Support for electrolyser and fuel-cell deployment, which drives these cost reductions through learning, is therefore a more effective instrument for diesel-free microgrids than carbon pricing alone.

4.5. Limitations and Future Work

The scope of the study and directions for future work are as follows. (i) Technical lifetimes, efficiencies and costs reflect current values; the effect of the cost multipliers of Table 1 is shown separately (Section 3.9). (ii) The load follows the national DEL benchmark for residential communities; metered profiles of specific buildings or communities can be inserted directly into the open model. (iii) Meteorological uncertainty is represented by the 10 historical years 2012–2021; more extreme conditions can be explored with a temporally coherent budget-of-uncertainty set [61] or synthetic weather years. (iv) The dispatch of the core model is optimised with perfect foresight within each year, as is standard in capacity planning; the operational layer of Section 2.7 adds unit commitment, operating reserve and wear, and forecast-based rolling operation can be added on this basis. (v) Dynamic stability,

component failures and black-start operation are the subject of dynamic and reliability models that can build on the designs reported here. (vi) For the DG-backed configurations, the optimality gaps of the two-stage procedure are reported in Table A1. (vii) The life-cycle boundary covers PV, wind and battery manufacturing; hydrogen equipment and upstream diesel supply can be added in a full life-cycle assessment. (viii) Employment is assessed with generic employment factors; local and embodied jobs are separated ex post (Section 2.4.4) with phase shares that are available only for PV, wind and the DG, and country-specific, phase-resolved factors for batteries and hydrogen equipment are needed before local employment can be optimised directly. Future work should apply stochastic and distributionally robust optimisation [34,35]; explore data-driven energy management [79,80]; evaluate novel battery chemistries and hydrogen carriers, such as ammonia [28,81]; integrate sector coupling in urban and industrial contexts; validate the results with pilot projects; and conduct life-cycle assessments covering resource extraction, recycling and circular-economy pathways.

Start–stop wear of the hydrogen chain. The wear model of Section 2.7 charges the electrolyser and the fuel cell for operating hours or throughput, but not for start–stop cycles, although the hydrogen chain starts frequently in the operational layer: the electrolyser 872, 552 and 203 times and the fuel cell 625, 440 and 146 times per year in A, B and E (Table 10). Thermal, pressure and potential cycling during start-up and shut-down accelerates membrane and catalyst degradation. As a sensitivity test, each start was charged an equivalent wear of h_s operating hours against the stack lives of 60,000 h (electrolyser) and 40,050 h (fuel cell), and the replacement schedule of the fixed operational designs was re-evaluated (operating hours were used as a conservative proxy for full-load hours where the latter are not reported). Because start–stop degradation rates of PEM stacks depend strongly on the stack design and on the start-up and shut-down procedure, h_s was varied parametrically over 2, 5 and 10 h. With $h_s = 2$ h, the lifetime cost rises by 1.3% (A), 1.0% (B) and 0.1% (E), mainly through the fuel cell; with $h_s = 5$ h, by 3.2%, 4.0% and 0.3%. With $h_s = 10$ h, the electrolyser stack of B reaches the end of its life after 7.5 instead of 16 years, so that two stack overhauls instead of one fall within the project lifetime, and the lifetime cost rises by 6.5% (A), 9.6% (B) and 0.9% (E). The hybrid E is barely affected, because its electrolyser runs for 14 h per start on average and its fuel cell starts rarely. The least-cost configuration C and the least-cost fully renewable configuration E keep their positions; only B and D, whose order already depends on the weather year (Section 3.12), change places at $h_s = 10$ h. Because the designs were not re-optimised, these values bound the cost increase from above: a model that prices start-up wear would reduce the number of starts, for example through minimum up and down times for the electrolyser and the fuel cell analogous to Equation (35). Their mean run lengths in Table 10 are already 2.7–14 h, so such constraints would bind mainly for the short fuel-cell runs of A.

5. Conclusions

This study compared hydrogen-based, battery-based and combined storage in five renewable microgrid configurations using an open, bus-resolved multi-objective MILP framework that considers total lifetime cost, GHG emissions and employment creation under deterministic and robust optimisation. All results are generated with open input data, and costs are expressed per unit of electricity delivered to the load. The main conclusions, which apply to the five structures considered, are as follows:

1. Expressed per kWh delivered, the cost of electricity ranges from 0.71 $/kWh (C, battery with DG backup) to 1.29 $/kWh (D, battery only) for the compromise designs. Normalising by generated electricity understates the cost by a factor of 4–7 and changes the ranking; on a served-energy basis, hydrogen-only storage is not the least-cost option.

2. DG backup substantially reduces the required renewable and storage capacity and therefore the cost, at the price of direct emissions and fuel dependence; constraining the DG emissions of the battery-based system to 10% of the least-cost value raises its lifetime cost by only 14%.
3. Among the fully renewable options, the co-optimised hydrogen–battery hybrid E is the least expensive (1.30 M$ versus 1.96 M$ for B and 2.06 M$ for D): the battery provides daily balancing and the hydrogen tank a reserve for prolonged multi-day deficits. At this scale, hydrogen does not act as seasonal storage.
4. All fully renewable configurations avoid the same operational emissions (3657 t CO_2e over 21 years) because they serve the same load; employment benefits (0.3–1.4 FTE jobs) scale with installed capacity, are highly uncertain for battery-based designs and include only 0.19–0.37 FTE of local installation and O&M jobs when storage equipment is imported.
5. Designs optimised for a single median year are not guaranteed to be adequate in other years; robust designs sized for all 10 historical years serve the load in every year, and their worst-case cost increases monotonically with the cost uncertainty level without changing the ranking of the configurations;
6. These findings are robust: with unit commitment, operating reserve and wear-based replacement the lifetime costs rise by 1–9% without changing the least-cost options, and C and E keep their positions across 10 design years, three additional load profiles, four site archetypes and joint sampling of all key inputs, whereas the order of the single-storage configurations B and D depends on the weather year;
7. Carbon prices at the level of the EU ETS make the diesel-free hybrid cheaper than the hydrogen–diesel configuration but not cheaper than the battery–diesel configuration, whereas a 75% reduction of hydrogen equipment costs makes the diesel-free hybrid as cheap as battery–diesel supply (0.61 versus 0.62 $/kWh).

Hydrogen storage therefore strengthens multi-day supply adequacy and decarbonisation when combined with batteries, whereas batteries with diesel backup remain the least-cost option at current costs; cost reductions of hydrogen equipment, more than carbon pricing, determine when diesel-free microgrids become the least-cost choice. Future research should extend the analysis to more extreme weather conditions, dynamic stability, life-cycle impacts and sector-coupled applications.

Supplementary Materials: The following supporting information can be downloaded at: https://www.mdpi.com/article/10.3390/su182211579/s1, Code S1: Python implementation of the model and post-processing scripts; Data S1: hourly meteorological input data (NASA POWER, 2011–2021), load profiles and derived hourly PV, wind and load series; Table S1: detailed results of all deterministic, Pareto, robust, sensitivity and scenario runs, including the operational back-tests.

Author Contributions: Conceptualisation, X.L. and H.G.; methodology, X.L. and H.G.; software, X.L.; validation, X.L., J.Z. and J.L.; formal analysis, X.L.; investigation, X.L. and J.Z.; data curation, C.F. and J.L.; writing—original draft preparation, X.L.; writing—review and editing, H.G.; visualisation, C.F. and J.L.; supervision, H.G.; project administration, H.G.; funding acquisition, H.G. All authors have read and agreed to the published version of the manuscript.

Funding: This research was funded by the Hainan Provincial Natural Science Foundation Young Scholars Fund Program (Research on the Theory and Method of Automatic Identification of Low-Voltage Distribution Network), grant number 124QN249.

Institutional Review Board Statement: Not applicable.

Informed Consent Statement: Not applicable.

Data Availability Statement: The hourly meteorological data were obtained from the NASA POWER service [37]; the load profiles are the open DEL benchmark profiles [40]. The complete input data, the model code and all numerical results are provided as Supplementary Materials (Code S1, Data S1 and Table S1) and allow every result of this study to be reproduced.

Conflicts of Interest: The authors declare no conflicts of interest.

Abbreviations

The following abbreviations are used in this manuscript:

BESS	Battery energy storage system
BoP	Balance of plant
DEL	Domestic Electrical Load (study)
DG	Diesel generator
DoD	Depth of discharge
ECF	Employment creation factor
EU ETS	European Union Emissions Trading System
FTE	Full-time equivalent
GGE	Greenhouse gas emissions (objective function)
GHG	Greenhouse gas
GHI	Global horizontal irradiance
HESS	Hydrogen energy storage system
HHV	Higher heating value
KPI	Key performance indicator
LCOE	Levelised cost of electricity
LHV	Lower heating value
LPSP	Loss-of-power-supply probability
LPT	Low-pressure hydrogen tank
MERRA-2	Modern-Era Retrospective analysis for Research and Applications, Version 2
MILP	Mixed-integer linear programming
NASA POWER	NASA Prediction of Worldwide Energy Resources
NOCT	Nominal operating cell temperature
NPV	Net present value
O&M	Operation and maintenance
PEM-EL	Proton exchange membrane electrolyser
PEM-FC	Proton exchange membrane fuel cell
PV	Photovoltaic
REPF	Renewable energy penetration factor
RES	Renewable energy sources
SDG	Sustainable Development Goal
SoC	State of charge
STC	Standard test conditions
TLC	Total lifetime cost
WT	Wind turbine

Appendix A

Table A1 lists the problem sizes, solution times and optimality gaps of the main optimisation runs.

Table A1. Problem sizes, solution times and optimality gaps.

Run	Variables	Constraints	Integer Variables	Wall Time (s)	Gap (%)
A, least cost (G50)	87,606	113,881	8762	1085	22.7 [1]
A, compromise (G10)	87,606	113,881	8762	855	4.0 [1]
B, least cost (min)	61,326	96,360	2	67	≤0.1
B, compromise (J50)	61,326	96,361	2	30	≤0.1
C, least cost (G50)	87,604	113,881	8762	804	5.9 [1]
C, compromise (G10)	87,604	113,881	8762	169	1.1 [1]
D, least cost (min)	61,324	96,360	2	18	≤0.1

Table A1. *Cont.*

Run	Variables	Constraints	Integer Variables	Wall Time (s)	Gap (%)
D, compromise (J50)	61,324	96,361	2	19	≤0.1
E, least cost (min)	87,607	140,160	2	180	≤0.1
E, compromise (J25)	87,607	140,161	2	150	≤0.1
A, robust $\delta = 11\%$ (2 yr)	175,207	–	–	3874	4.9 [1]
A, robust $\delta = 21\%$ (2 yr)	175,207	–	–	4165	4.9 [1]
A, robust $\delta = 31\%$ (2 yr)	175,207	–	–	3578	4.3 [1]
A, robust $\delta = 41\%$ (2 yr)	175,207	–	–	4333	4.9 [1]
B, robust $\delta = 11\%$ (2 yr)	122,647	–	–	315	≤0.1
B, robust $\delta = 21\%$ (2 yr)	122,647	–	–	242	≤0.1
B, robust $\delta = 31\%$ (2 yr)	122,647	–	–	214	≤0.1
B, robust $\delta = 41\%$ (2 yr)	122,647	–	–	203	≤0.1
C, robust $\delta = 11\%$ (2 yr)	175,205	–	–	1620	1.8 [1]
C, robust $\delta = 21\%$ (2 yr)	175,205	–	–	1178	1.8 [1]
C, robust $\delta = 31\%$ (2 yr)	175,205	–	–	941	1.8 [1]
C, robust $\delta = 41\%$ (2 yr)	175,205	–	–	1735	1.8 [1]
D, robust $\delta = 11\%$ (2 yr)	122,645	–	–	97	≤0.1
D, robust $\delta = 21\%$ (2 yr)	122,645	–	–	52	≤0.1
D, robust $\delta = 31\%$ (2 yr)	122,645	–	–	58	≤0.1
D, robust $\delta = 41\%$ (2 yr)	122,645	–	–	54	≤0.1
E, robust $\delta = 11\%$ (3 yr)	262,808	–	–	1833	≤0.1
E, robust $\delta = 21\%$ (3 yr)	262,808	–	–	1039	≤0.1
E, robust $\delta = 31\%$ (3 yr)	262,808	–	–	1085	≤0.1
E, robust $\delta = 41\%$ (3 yr)	262,808	–	–	1324	≤0.1

Solver: HiGHS via SciPy 1.18.1; two virtual CPUs (Intel Xeon, 2.1 GHz), 7.6 GB RAM. Configurations B, D and E were solved to a relative MIP gap of at most 0.1%. [1] For the DG-backed configurations, the gap is the upper bound $(UB - LB)/UB$ between the best feasible design (two-stage procedure, unit-commitment MILP solved to 0.2%) and the stage-1 lower bound with relaxed commitment; robust times include the back-tests of all constraint-generation iterations.

References

1. Kalair, A.; Abas, N.; Saleem, M.S.; Kalair, A.R.; Khan, N. Role of Energy Storage Systems in Energy Transition from Fossil Fuels to Renewables. *Energy Storage* **2021**, *3*, e135. [CrossRef]
2. Suraparaju, S.K.; Samykano, M.; Vennapusa, J.R.; Rajamony, R.K.; Balasubramanian, D.; Said, Z.; Pandey, A.K. Challenges and Prospectives of Energy Storage Integration in Renewable Energy Systems for Net Zero Transition. *J. Energy Storage* **2025**, *125*, 116923. [CrossRef]
3. Yánez-Rosales, P.; Schallenberg-Rodríguez, J.; del Río-Gamero, B. A Methodological Procedure for the Energy Transition in the Land Transport Sector by Quantifying Renewable Energy Needs. *Energy Rep.* **2025**, *13*, 6042–6058. [CrossRef]
4. Harpprecht, C.; Naegler, T.; Steubing, B.; Tukker, A.; Simon, S. Decarbonization Scenarios for the Iron and Steel Industry in Context of a Sectoral Carbon Budget: Germany as a Case Study. *J. Clean. Prod.* **2022**, *380*, 134846. [CrossRef]
5. Lee, H.; McJeon, H.; Yu, S.; Liu, Y.; Kim, H.; Eom, J. Decarbonization Pathways for Korea's Industrial Sector towards Its 2050 Carbon Neutrality Goal. *J. Clean. Prod.* **2024**, *476*, 143749. [CrossRef]
6. IEA; IRENA; UNSD; World Bank; WHO. *Tracking SDG 7: The Energy Progress Report 2025*; World Bank: Washington, DC, USA, 2025.
7. Energy Institute. *Statistical Review of World Energy 2024*, 73rd ed.; Energy Institute: London, UK, 2024.
8. Hosan, S.; Sen, K.K.; Rahman, M.M.; Karmaker, S.C.; Chapman, A.J.; Saha, B.B. Mitigating Energy Poverty: A Panel Analysis of Energy Policy Interventions in Emerging Economies of the Asia-Pacific Region. *Energy* **2024**, *291*, 130367. [CrossRef]
9. Arsad, A.Z.; Hannan, M.A.; Al-Shetwi, A.Q.; Mansur, M.; Muttaqi, K.M.; Dong, Z.Y.; Blaabjerg, F. Hydrogen Energy Storage Integrated Hybrid Renewable Energy Systems: A Review Analysis for Future Research Directions. *Int. J. Hydrogen Energy* **2022**, *47*, 17285–17312. [CrossRef]
10. Iris, Ç.; Lam, J.S.L. Optimal Energy Management and Operations Planning in Seaports with Smart Grid while Harnessing Renewable Energy under Uncertainty. *Omega* **2021**, *103*, 102445. [CrossRef]
11. Shirwani, R.; Gulzar, S.; Asim, M.; Umair, M.; Al-Rashid, M.A. Control of Vehicular Emission Using Innovative Energy Solutions Comprising of Hydrogen for Transportation Sector in Pakistan: A Case Study of Lahore City. *Int. J. Hydrogen Energy* **2020**, *45*, 16287–16297. [CrossRef]
12. Ishaq, M.; Dincer, I. A Novel Integrated Gas-Cooled Fast Nuclear Reactor and Vanadium Chloride Thermochemical Cycle for Sustainable Fuel Production. *J. Clean. Prod.* **2024**, *468*, 142853. [CrossRef]

13. Mößle, P.; Herrmannsdörfer, T.; Welzl, M.; Brüggemann, D.; Danzer, M.A. Economic Optimization for the Dynamic Operation of a Grid Connected and Battery-Supported Electrolyzer. *Int. J. Hydrogen Energy* **2025**, *100*, 749–759. [CrossRef]
14. Trivedi, A.; Trivedi, V.; Singh, R. Road to Decarbonization: Navigating India's Green Hydrogen Transition Challenges through Grey DEMATEL. *J. Clean. Prod.* **2025**, *486*, 144502. [CrossRef]
15. Stoter, J.; Tang, X.; Cvetkovic, M.; Palensky, P.; Polinder, H.; Iris, Ç.; Schulte, F. Energy Management and Stochastic Operations Planning for Electrified Container Terminals with Uncertain Energy Supply and Demand. *J. Clean. Prod.* **2025**, *527*, 146383. [CrossRef]
16. Doytch, N.; Narayan, S. Does Transitioning towards Renewable Energy Accelerate Economic Growth? An Analysis of Sectoral Growth for a Dynamic Panel of Countries. *Energy* **2021**, *235*, 121290. [CrossRef]
17. Tenaw, D. Do Traditional Energy Dependence, Income, and Education Matter in the Dynamic Linkage between Clean Energy Transition and Economic Growth in Sub-Saharan Africa? *Renew. Energy* **2022**, *193*, 204–213. [CrossRef]
18. Rutovitz, J.; Dominish, E.; Downes, J. *Calculating Global Energy Sector Jobs: 2015 Methodology*; Institute for Sustainable Futures, University of Technology Sydney: Sydney, Australia, 2015.
19. Kumar, N.; Karmakar, S. Techno-Economic Optimization of Hydrogen Generation through Hybrid Energy System: A Step towards Sustainable Development. *Int. J. Hydrogen Energy* **2024**, *55*, 400–413. [CrossRef]
20. Song, H.; Guo, H.; Wang, Y.; Lao, J.; Zhu, H.; Tang, L.; Liu, X. A Novel Hybrid Energy System for Hydrogen Production and Storage in a Depleted Oil Reservoir. *Int. J. Hydrogen Energy* **2021**, *46*, 18020–18031. [CrossRef]
21. Kang, J.-N.; Liu, L.; Liu, L.-C.; Wei, Y.-M. Operation Strategy for a Net-Zero Emissions Park Microgrid with Multi-Stakeholders: A Multi-Objective with Bi-Level Optimization Approach. *Energy* **2025**, *321*, 135524. [CrossRef]
22. Ebrahimi, S.R.; Rahimiyan, M.; Assili, M.; Hajizadeh, A. Energy Management of Net-Zero Energy Buildings: A Two-Layer Hierarchical Approach. *Energy Build.* **2025**, *336*, 115592. [CrossRef]
23. Tian, T.; Ma, Z.; Pan, T.; Wu, C.; Shu, J.; Feng, R.; Ding, J. Storage Dimensioning and Energy Management for a Grid-Connected Wind/PV/Hydrogen/Battery System Using MISOCP Approach. *Int. J. Hydrogen Energy* **2025**, *100*, 779–791. [CrossRef]
24. Katla, D.; Bartela, Ł.; Skorek-Osikowska, A. Evaluation of Electricity Generation Subsystem of Power-to-Gas-to-Power Unit Using Gas Expander and Heat Recovery Steam Generator. *Energy* **2020**, *212*, 118600. [CrossRef]
25. Li, Y.; Wang, K.; Sun, Q. Experimental Investigations on the Dynamic Transport Characteristics of H_2, CO_2, and CH_4 Gas Mixtures in Shale: Implications for Underground Hydrogen Storage. *Int. J. Hydrogen Energy* **2025**, *138*, 582–594. [CrossRef]
26. Kim, C.; Devegowda, D.; Dang, S.T.; Mehana, M. Modeling the Diffusivity of Hydrogen and the Associated Cushion Gas in Depleted Hydrocarbon Reservoir Caprocks. *Int. J. Hydrogen Energy* **2025**, *105*, 248–257. [CrossRef]
27. Osman, A.I.; Ayati, A.; Farrokhi, M.; Khadempir, S.; Rajabzadeh, A.R.; Farghali, M.; Krivoshapkin, P.; Tanhaei, B.; Rooney, D.W.; Yap, P.-S. Innovations in Hydrogen Storage Materials: Synthesis, Applications, and Prospects. *J. Energy Storage* **2024**, *95*, 112376. [CrossRef]
28. Rossetti, I.; Tripodi, A.; Tommasi, M.; Ramis, G. Conceptual Design of a Process for Hydrogen Production from Waste Biomass and Its Storage in Form of Liquid Ammonia. *Int. J. Hydrogen Energy* **2023**, *48*, 37443–37460. [CrossRef]
29. Datta, U.; Kalam, A.; Shi, J. A Review of Key Functionalities of Battery Energy Storage System in Renewable Energy Integrated Power Systems. *Energy Storage* **2021**, *3*, e224. [CrossRef]
30. Calise, F.; Cappiello, F.L.; Cimmino, L.; Dentice d'Accadia, M.; Vicidomini, M. Renewable Smart Energy Network: A Thermoeconomic Comparison between Conventional Lithium-Ion Batteries and Reversible Solid Oxide Fuel Cells. *Renew. Energy* **2023**, *214*, 74–95. [CrossRef]
31. Lokar, J.; Virtič, P. The Potential for Integration of Hydrogen for Complete Energy Self-Sufficiency in Residential Buildings with Photovoltaic and Battery Storage Systems. *Int. J. Hydrogen Energy* **2020**, *45*, 34566–34578. [CrossRef]
32. Berna-Escriche, C.; Vargas-Salgado, C.; Alfonso-Solar, D.; Escrivá-Castells, A. Can a Fully Renewable System with Storage Cost-Effectively Cover the Total Demand of a Big Scale Standalone Grid? Analysis of Three Scenarios Applied to the Grand Canary Island, Spain by 2040. *J. Energy Storage* **2022**, *52*, 104774. [CrossRef]
33. Wang, B.; Ba, Z. Hydrogen Energy Storage: Mitigating Variability in Wind and Solar Power for Grid Stability in Australia. *Int. J. Hydrogen Energy* **2025**, *97*, 1249–1260. [CrossRef]
34. Fan, J.; Yan, R.; He, Y.; Zhang, J.; Zhao, W.; Liu, M.; An, S.; Ma, Q. Stochastic Optimization of Combined Energy and Computation Task Scheduling Strategies of Hybrid System with Multi-Energy Storage System and Data Center. *Renew. Energy* **2025**, *242*, 122466. [CrossRef]
35. Cai, P.; Wen, C.; Cao, B.; Qiao, J. A Wasserstein Metric Distributionally Robust Chance-Constrained Peer Aggregation Energy Sharing Mechanism for Hydrogen-Based Microgrids Considering Low-Carbon Drivers. *Energy* **2025**, *325*, 136178. [CrossRef]
36. McCauley, D.; Pettigrew, K. Building a Just Transition in Asia-Pacific: Four Strategies for Reducing Fossil Fuel Dependence and Investing in Clean Energy. *Energy Policy* **2023**, *183*, 113808. [CrossRef]
37. NASA Langley Research Center. Prediction of Worldwide Energy Resources (POWER) Project, Hourly Data Services. Available online: https://power.larc.nasa.gov/ (accessed on 30 October 2026).

38. Gelaro, R.; McCarty, W.; Suárez, M.J.; Todling, R.; Molod, A.; Takacs, L.; Randles, C.A.; Darmenov, A.; Bosilovich, M.G.; Reichle, R.; et al. The Modern-Era Retrospective Analysis for Research and Applications, Version 2 (MERRA-2). *J. Clim.* **2017**, *30*, 5419–5454. [CrossRef] [PubMed]
39. Duffie, J.A.; Beckman, W.A. *Solar Engineering of Thermal Processes*, 4th ed.; John Wiley & Sons: Hoboken, NJ, USA, 2013.
40. Toussaint, W.; Moodley, D. Clustering Residential Electricity Consumption Data to Create Archetypes that Capture Household Behaviour in South Africa. *S. Afr. Comput. J.* **2020**, *32*, 1–34. Available online: https://github.com/wiebket/delarchetypes (accessed on 30 October 2026). [CrossRef]
41. *IEC 61724-1:2021*; Photovoltaic System Performance—Part 1: Monitoring. International Electrotechnical Commission: Geneva, Switzerland, 2021.
42. *IEC 60904-3:2019*; Photovoltaic Devices—Part 3: Measurement Principles for Terrestrial Photovoltaic (PV) Solar Devices with Reference Spectral Irradiance Data. International Electrotechnical Commission: Geneva, Switzerland, 2019.
43. *IEC 61215-2:2016*; Terrestrial Photovoltaic (PV) Modules—Design Qualification and Type Approval—Part 2: Test Procedures. International Electrotechnical Commission: Geneva, Switzerland, 2016.
44. Manwell, J.F.; McGowan, J.G.; Rogers, A.L. *Wind Energy Explained: Theory, Design and Application*, 2nd ed.; John Wiley & Sons: Chichester, UK, 2009.
45. Sdanghi, G.; Maranzana, G.; Celzard, A.; Fierro, V. Review of the Current Technologies and Performances of Hydrogen Compression for Stationary and Automotive Applications. *Renew. Sustain. Energy Rev.* **2019**, *102*, 150–170. [CrossRef]
46. Maru, H.; Singhal, S.C.; Stone, C.; Wheeler, D. *1–10 kW Stationary Combined Heat and Power Systems Status and Technical Potential: Independent Review*; NREL/BK-6A10-48265; National Renewable Energy Laboratory: Golden, CO, USA, 2010.
47. Short, W.; Packey, D.J.; Holt, T. *A Manual for the Economic Evaluation of Energy Efficiency and Renewable Energy Technologies*; NREL/TP-462-5173; National Renewable Energy Laboratory: Golden, CO, USA, 1995.
48. Gómez, D.R.; Watterson, J.D.; Americano, B.B.; Ha, C.; Marland, G.; Matsika, E.; Namayanga, L.N.; Osman-Elasha, B.; Saka, J.D.K.; Treanton, K. Stationary Combustion. In *2006 IPCC Guidelines for National Greenhouse Gas Inventories*; Eggleston, H.S., Buendia, L., Miwa, K., Ngara, T., Tanabe, K., Eds.; IGES: Hayama, Japan, 2006; Volume 2, Chapter 2.
49. Department of Forestry, Fisheries and the Environment. *South Africa's 2024 Grid Emission Factors Report*; Government Notice No. 7891, Government Gazette No. 55353; Republic of South Africa: Pretoria, South Africa, 2026.
50. Republic of South Africa. *Carbon Tax Act No. 15 of 2019*; Government Gazette No. 42483; Republic of South Africa: Pretoria, South Africa, 23 May 2019.
51. National Treasury. *Budget Review 2026*; National Treasury, Republic of South Africa: Pretoria, South Africa, 2026.
52. Schlömer, S.; Bruckner, T.; Fulton, L.; Hertwich, E.; McKinnon, A.; Perczyk, D.; Roy, J.; Schaeffer, R.; Sims, R.; Smith, P.; et al. Annex III: Technology-Specific Cost and Performance Parameters. In *Climate Change 2014: Mitigation of Climate Change. Contribution of Working Group III to the Fifth Assessment Report of the Intergovernmental Panel on Climate Change*; Edenhofer, O., Pichs-Madruga, R., Sokona, Y., Farahani, E., Kadner, S., Seyboth, K., Adler, A., Baum, I., Brunner, S., Eickemeier, P., et al., Eds.; Cambridge University Press: Cambridge, UK; New York, NY, USA, 2014; pp. 1329–1356.
53. Emilsson, E.; Dahllöf, L. *Lithium-Ion Vehicle Battery Production: Status 2019 on Energy Use, CO_2 Emissions, Use of Metals, Products Environmental Footprint, and Recycling*; Report C444; IVL Swedish Environmental Research Institute: Stockholm, Sweden, 2019.
54. Yang, H.; Zhou, W.; Lu, L.; Fang, Z. Optimal Sizing Method for Stand-Alone Hybrid Solar–Wind System with LPSP Technology by Using Genetic Algorithm. *Sol. Energy* **2008**, *82*, 354–367. [CrossRef]
55. Marler, R.T.; Arora, J.S. The Weighted Sum Method for Multi-Objective Optimization: New Insights. *Struct. Multidiscip. Optim.* **2010**, *41*, 853–862. [CrossRef]
56. Mavrotas, G. Effective Implementation of the ε-Constraint Method in Multi-Objective Mathematical Programming Problems. *Appl. Math. Comput.* **2009**, *213*, 455–465. [CrossRef]
57. Virtanen, P.; Gommers, R.; Oliphant, T.E.; Haberland, M.; Reddy, T.; Cournapeau, D.; Burovski, E.; Peterson, P.; Weckesser, W.; Bright, J.; et al. SciPy 1.0: Fundamental Algorithms for Scientific Computing in Python. *Nat. Methods* **2020**, *17*, 261–272. [CrossRef] [PubMed]
58. Huangfu, Q.; Hall, J.A.J. Parallelizing the Dual Revised Simplex Method. *Math. Program. Comput.* **2018**, *10*, 119–142. [CrossRef]
59. Ben-Tal, A.; El Ghaoui, L.; Nemirovski, A. *Robust Optimization*; Princeton University Press: Princeton, NJ, USA, 2009.
60. Zeng, B.; Zhao, L. Solving Two-Stage Robust Optimization Problems Using a Column-and-Constraint Generation Method. *Oper. Res. Lett.* **2013**, *41*, 457–461. [CrossRef]
61. Bertsimas, D.; Sim, M. The Price of Robustness. *Oper. Res.* **2004**, *52*, 35–53. [CrossRef]
62. Buttler, A.; Spliethoff, H. Current Status of Water Electrolysis for Energy Storage, Grid Balancing and Sector Coupling via Power-to-Gas and Power-to-Liquids: A Review. *Renew. Sustain. Energy Rev.* **2018**, *82*, 2440–2454. [CrossRef]
63. HOMER Energy. Required Operating Capacity (Operating Reserve). HOMER Knowledge Base. Available online: https://homerenergy.com/docs/knowledgebase/article/required-operating-capacity-operating-reserve/ (accessed on 1 November 2026).

64. Viswanathan, V.; Mongird, K.; Franks, R.; Li, X.; Sprenkle, V.; Baxter, R. *2022 Grid Energy Storage Technology Cost and Performance Assessment*; PNNL-33283; Pacific Northwest National Laboratory: Richland, WA, USA, 2022.
65. IRENA. *Green Hydrogen Cost Reduction: Scaling Up Electrolysers to Meet the 1.5 °C Climate Goal*; International Renewable Energy Agency: Abu Dhabi, United Arab Emirates, 2020.
66. GMK Center. European Carbon Prices Rose to €88/t in October. 15 October 2026. Available online: https://gmk.center/en/news/european-carbon-prices-rose-to-e88-t-in-october/ (accessed on 1 November 2026).
67. U.S. Environmental Protection Agency. *Report on the Social Cost of Greenhouse Gases: Estimates Incorporating Recent Scientific Advances*; EPA: Washington, DC, USA, 2023.
68. Alharbi, A.M.; Ali, Z.M.; Diab, A.A.Z. Comparative Techno-Economic Optimization of Microgrid Configurations Using Hybrid Battery–Hydrogen Storage: NEOM Case Study, Saudi Arabia. *PLoS ONE* **2025**, *20*, e0326050. [CrossRef] [PubMed]
69. Kalinci, Y.; Hepbasli, A.; Dincer, I. Techno-Economic Analysis of a Stand-Alone Hybrid Renewable Energy System with Hydrogen Production and Storage Options. *Int. J. Hydrogen Energy* **2015**, *40*, 7652–7664. [CrossRef]
70. Dawood, F.; Shafiullah, G.M.; Anda, M. Stand-Alone Microgrid with 100% Renewable Energy: A Case Study with Hybrid Solar PV-Battery-Hydrogen. *Sustainability* **2020**, *12*, 2047. [CrossRef]
71. Trapani, D.; Marocco, P.; Ferrero, D.; Lindberg, K.B.; Sundseth, K.; Santarelli, M. The Potential of Hydrogen-Battery Storage Systems for a Sustainable Renewable-Based Electrification of Remote Islands in Norway. *J. Energy Storage* **2024**, *75*, 109482. [CrossRef]
72. Shahverdian, M.H.; Soltanifar, F.; Sohani, A.; Sayyaadi, H.; Hoseinzadeh, S. A 3E Comparative Study to Choose the Best Storage Method for PV Solar System for Off-Grid Applications: Hydrogen or Battery? *J. Energy Storage* **2025**, *117*, 116111. [CrossRef]
73. Madziga, M.; Rahil, A.; Mansoor, R. Comparison between Three Off-Grid Hybrid Systems (Solar Photovoltaic, Diesel Generator and Battery Storage System) for Electrification for Gwakwani Village, South Africa. *Environments* **2018**, *5*, 57. [CrossRef]
74. Zhao, C.; Dong, K.; Wang, K.; Nepal, R. How Does Artificial Intelligence Promote Renewable Energy Development? The Role of Climate Finance. *Energy Econ.* **2024**, *133*, 107493. [CrossRef]
75. Forrester, S.P.; Reames, T.G. Understanding the Residential Energy Efficiency Financing Coverage Gap and Market Potential. *Appl. Energy* **2020**, *260*, 114307. [CrossRef]
76. Samour, A.; Shahzad, U.; Mentel, G. Moving toward Sustainable Development: Assessing the Impacts of Taxation and Banking Development on Renewable Energy in the UAE. *Renew. Energy* **2022**, *200*, 706–713. [CrossRef]
77. Przychodzeń, W.; Przychodzeń, J. Determinants of Renewable Energy Production in Transition Economies: A Panel Data Approach. *Energy* **2020**, *191*, 116583. [CrossRef]
78. Li, K.; Tan, X.; Yan, Y.; Jiang, D.; Qi, S. Directing Energy Transition toward Decarbonization: The China Story. *Energy* **2022**, *261*, 124934. [CrossRef]
79. SaberiKamarposhti, M.; Kamyab, H.; Krishnan, S.; Yusuf, M.; Rezania, S.; Chelliapan, S.; Khorami, M. A Comprehensive Review of AI-Enhanced Smart Grid Integration for Hydrogen Energy: Advances, Challenges, and Future Prospects. *Int. J. Hydrogen Energy* **2024**, *67*, 1009–1025. [CrossRef]
80. Entezari, A.; Aslani, A.; Zahedi, R.; Noorollahi, Y. Artificial Intelligence and Machine Learning in Energy Systems: A Bibliographic Perspective. *Energy Strategy Rev.* **2023**, *45*, 101017. [CrossRef]
81. Vincent, M.; Castilla-Martinez, C.A.; Janot, R.; Demirci, U.B. Exploring the Potential of Ammonia Alane AlH3NH3 as Hydrogen Carrier. *Int. J. Hydrogen Energy* **2024**, *74*, 101–111. [CrossRef]

Disclaimer/Publisher's Note: The statements, opinions and data contained in all publications are solely those of the individual author(s) and contributor(s) and not of MDPI and/or the editor(s). MDPI and/or the editor(s) disclaim responsibility for any injury to people or property resulting from any ideas, methods, instructions or products referred to in the content.